



1 **PyRTlib: an educational Python-based library for non-scattering** 2 **atmospheric microwave Radiative Transfer computations**

3 Salvatore Larosa¹, Domenico Cimini^{1,2}, Donatello Gallucci¹, Saverio Teodosio Nilo¹, and Filomena
4 Romano¹

5 ¹National Research Council of Italy, Institute of Methodologies for Environmental Analysis (CNR-IMAA), Tito Scalo
6 (Potenza), 85050, Italy

7 ²CETEMPS, University of L'Aquila, L'Aquila, 67100, Italy

8 *Correspondence to:* Salvatore Larosa (salvatore-larosa@cnr.it)

9 **Abstract.** This article introduces PyRTlib, a new standalone Python package for non-scattering line-by-line microwave
10 Radiative Transfer simulations. PyRTlib is a flexible and user-friendly tool for computing down and up-welling brightness
11 temperatures and related quantities (e.g., atmospheric absorption, optical depth, opacity, mean radiating temperature) written
12 in Python, a language commonly used nowadays for scientific software development especially by students and early career
13 scientists. PyRTlib allows simulating observations from ground-based, airborne, and satellite microwave sensors in clear sky
14 and in cloudy conditions (under non-scattering Rayleigh approximation). The intention for PyRTlib is not to be a competitor
15 for state-of-the-art atmospheric radiative transfer codes that excel for speed and/or versatility (e.g., ARTS, RTTOV). The
16 intention is to provide an educational tool, completely written in Python, to readily simulate atmospheric microwave radiative
17 transfer from a variety of input profiles, including predefined climatologies, global radiosonde archives, and model reanalysis.
18 The paper presents quick examples for the built in modules to access popular open data archives. The paper also presents
19 examples for computing simulated brightness temperature for different platforms (ground-based, airborne, and satellite), using
20 various input profiles, showing how to easily modify other relevant parameters, such as observing angle (zenith, nadir, slant),
21 surface emissivity, and gas absorption model. PyRTlib can be easily embedded in other Python codes needing atmospheric
22 microwave radiative transfer (e.g., surface emissivity models and retrievals). Despite its simplicity, PyRTlib can be readily
23 used to produce present-day scientific results, as demonstrated by two examples showing (*i*) absorption model comparison and
24 validation with ground-based radiometric observations and (*ii*) uncertainty propagation of spectroscopic parameters through
25 the radiative transfer calculations following a rigorous approach. To our knowledge, the uncertainty estimate is not provided
26 by any other currently available microwave radiative transfer code, making PyRTlib unique for this aspect in the atmospheric
27 microwave radiative transfer code scenario.

28



29 **1 Introduction**

30 Radiative transfer (RT) models play a fundamental role in atmospheric sciences, as they are broadly used to simulate how
31 electromagnetic radiation travels through the atmosphere as it interacts with atmospheric constituents (such as gases, aerosols
32 and hydrometeors) through absorption, emission, scattering, and refraction. RT models are commonly used as forward
33 operators to simulate and understand remote sensing observations from any platform, ground-based, airborne or spaceborne.
34 RT calculations depend on the state of the atmosphere (pressure, temperature, composition), the optical properties of the
35 atmospheric constituents (molecules and particles), the simulated observing geometry, and the spectral range. Given a set of
36 specifications on spectral range, atmospheric conditions, and observing geometry, the RT model is able to compute the
37 atmospheric opacity and the observations simulated accordingly. Simulated observations are then used in a broad range of
38 applications, from atmospheric process understanding, the retrieval of atmospheric variables, to data assimilation into
39 Numerical Weather Prediction (NWP) models. Although the theoretical aspects of wave-atmosphere interactions are
40 essentially the same throughout the electromagnetic spectrum, different RT models have been developed to account for the
41 specific features of limited spectral ranges, such as the visible, infrared, and microwave portions of the electromagnetic
42 spectrum. In particular, several microwave (MW) RT models have been developed throughout the years to serve the needs of
43 passive remote sensing from MW radiometers (e.g., Liebe, 1989; Buehler et al., 2005; Rosenkranz, 2017). Many examples are
44 available in the open literature on the use of MW RT models for atmospheric sciences, including but not limited to: process
45 understanding (Tripoli et al., 2005; Martinet et al 2017), atmospheric retrieval development (Eriksson et al., 2005; Boukabara
46 et al., 2013; Sanò et al., 2015; Larosa et al., 2023), MW instrument design and validation (Buehler et al., 2012; Fox et al.,
47 2017), data assimilation into NWP model (Eyre et al., 2020; Martinet et al., 2020), instrument synergy (Marzano et al., 1999;
48 Turner and Löhnert, 2021; Cimini et al., 2023). A variety of software codes has been developed throughout the past three
49 decades for implementing different flavours of available MW RT models, differing for features, assumptions, approximations,
50 as well as coding languages. Among the different features, RT codes may be classified in scattering or non-scattering (i.e.,
51 considering absorption only). Similarly, RT codes may be classified as line-by-line, meaning that RT can be modelled at any
52 frequency from the contributions of many gas absorption lines, or parameterized, meaning that RT can be modelled at a limited
53 number of channels for which the optical depth is parameterized considering their spectral response function, initially trained
54 with line-by-line calculations. Other assumptions include the observing geometry, going from plane-parallel one dimensional
55 (1-D) calculations that consider the atmosphere state changing only in the vertical dimension, to higher dimensional (2-D or
56 3-D) geometries, which allow to consider also the horizontal spatial dishomogeneity, to spherical geometry, allowing to
57 properly model the atmospheric shape and its effect on the bending angle of the radiation path. Although RT codes enabling
58 line-by-line, scattering, and spherical geometry computations are much more complex and computational demanding than the
59 parametrized, non-scattering, and 1-D plane-parallel assumptions, they allow more accurate modelling of the impact of spectral
60 resolution, particle size, and 3-D distribution, respectively. Concerning the coding language, most of MW RT software codes
61 are available in compiled programming languages such as C, C++ and Fortran. However, the interpreted programming



62 language Python has become increasingly popular for scientific computing in the last decades, thanks to its numerous extension
 63 packages, and it is now widely considered the language of choice in many areas, including atmospheric science. Therefore,
 64 some of the available RT codes allow users to access their features by running Python modules as wrapper of the core software,
 65 although the core software needs to be compiled from source or in binary form to access such modules. There are also cases
 66 for which the original code has been translated into Python. Table 1.1 reports a list of most popular MW RT codes, by no
 67 means complete, with their key features and access information. In the following, a brief introduction is given of the most
 68 relevant MW RT codes for this paper.

70 **Table 1.1:** List of popular codes suitable for atmospheric radiative transfer in the microwave spectral region.

Name	References	line-by-line/band	Scattering	Language	License	Access
ARTS	Eriksson et al., 2011; Buehler et al., 2018	line-by-line	Yes	C++ (python interface as wrapper)	GPL v3	https://www.radiativetransfer.org/
CRTM	Han et al., 2006; Ding et al., 2011; Wei et al., 2022	line-by-line/band	Yes	Fortran (python interface as wrapper)	CC0 v1.0	https://www.jcsda.org/jcsda-project-community-radiative-transfer-model
MonoRTM	Clough et al., 2005	line-by-line	Yes	Fortran	GPL	http://rtweb.aer.com/monortm_frame.html
PAMTRA	Mech et al., 2020	line-by-line	Yes	Fortran (python interface as wrapper)	GPL v3	https://pamtra.readthedocs.io/
Py4CATS	Schreier et al, 2019	line-by-line	No	Python	GPL	https://atmos.eoc.dlr.de/tools/Py4CATS/
RTTOV	Saunders et al., 2018	band	Yes	Fortran (python interface as wrapper)	available on request	https://nwp-saf.eumetsat.int/site/software/rttov/
RTTOV-gb	De Angelis et al., 2016 Cimini et al., 2019	line-by-line and band	Yes	Fortran	available on request	https://nwp-saf.eumetsat.int/site/software/rttov-gb/
TBUPDN	Rosenkranz, 2017	line-by-line and band	No	Fortran	freely available	http://cetemps.aquila.infn.it/rttovgb/lblmrt_ns.html

71
 72 **ARTS:** The Atmospheric Radiative Transfer Simulator (ARTS) is a radiative transfer model suitable for calculations from the
 73 microwave to the thermal infrared spectral range (Buehler et al., 2005; Eriksson et al., 2011; Buehler et al., 2018). ARTS is



74 implemented in C++ with a modular design, allowing the flexibility for performing many different applications concerning
75 radiative transfer calculations in all viewing geometries from inside or outside the atmosphere: uplooking, downlooking, limb-
76 looking. ARTS allows the choice of different state of the art absorption models, including line-by-line from HITRAN or other
77 catalogues plus various absorption continuum parameterizations. It is fully polarized, allowing RT calculations from 1 to 4
78 Stokes components. It allows scattering computations from spherical and non-spherical atmospheric particles. It also provides
79 analytical or semi-analytical Jacobians for a large set of state parameters. It supports XML and NetCDF file format for data
80 import and export. ARTS can be run standalone or through external tools, such as PyARTS, a Python package that serves as
81 wrapper for the main ARTS core library. PyARTS is part of the ARTS source repository. PyARTS provides an interactive
82 interface to the ARTS engine for running radiative transfer simulations and has many ARTS built-in types for the manipulation
83 of input data and the evaluation simulation results. However, PyARTS cannot be run as a standalone python package as it
84 needs ARTS built before.

85

86 **CRTM:** The Community Radiative Transfer Model (CRTM; Han et al., 2006; Ding et al., 2011; Wei et al., 2022) is a fast
87 radiative transfer model developed to efficiently simulate specific spaceborne Earth observing sensors. The CRTM was
88 developed by the U.S. Joint Center for Satellite Data Assimilation (JCSDA) to be a library for users to link to from other
89 models. However, CRTM can be run in "stand-alone" mode. CRTM is a sensor-based RT model, supporting more than 100
90 sensors on meteorological and other remote sensing satellites, covering wavelengths ranging from the visible through the
91 microwave. The source code is written in standard Fortran95 and makes extensive use of modules and derived type data
92 structures. CRTM includes both the forward model and its Jacobian with respect to the input atmospheric state variables,
93 accounting for the absorption of atmospheric gases as well as the multiple scattering of water and ice clouds composed of
94 spherical and a variety of nonspherical particles, working under all atmospheric and surface conditions. CRTM is extensively
95 used in several applications, such as the NOAA Microwave Integrated Retrieval System (MiRS), the NCEP data assimilation
96 system, and the NOAA STAR Integrated Calibration/Validation System Long-Term Monitoring System. CRTM can be called
97 from Python scripts using pyCRTM, which embeds CRTM Fortran data structures and procedures directly into Python, taking
98 advantage of both the simplicity and ease of use of Python syntax and the flexibility that comes from the extensive Python
99 ecosystem (Karpowicz et al., 2022).

100

101 **MonoRTM:** MonoRTM represents an atmospheric radiative transfer model widely used in the scientific community to
102 generate simulated spectral radiance ranging from the ultraviolet to the microwave region (Clough et al, 2005). It has been
103 produced by the Atmospheric & Environmental Research (AER) and is based on the same physical properties and continuum
104 absorption model as the Line-By-Line Radiative Transfer Model (LBLRTM), which is also developed and maintained by AER.
105 These are both Fortran 90 codes, however MonoRTM is particularly suitable to simulate a single or a set of few monochromatic
106 wavelengths. Atmospheric molecular absorption covers all spectral regions, with molecular optical depths computed within
107 the Monochromatic Optical Depth Model module; however, spectral radiance calculation in the presence of cloud liquid water



108 is only possible in the microwave range and relies on the model developed by Liebe et al. (1991). MonoRTM also accounts
109 for molecular absorption within the spectral line center, by using the MT_CKD continuum (Clough et al., 2005). Line coupling
110 effects, which are crucial for e.g., oxygen lines in the microwave region, are also dealt with in the code (Rosenkranz, 1988;
111 Tretyakov et al., 2005; Cadeddu et al., 2007).

112

113 **PAMTRA:** This is an atmospheric radiative transfer code, namely the Passive and Active Microwave radiative TRANSfer
114 (PAMTRA, Mech et al., 2020), specifically designed to simulate both passive microwave radiances as well as active remote
115 sensing measurements in the presence of cloudy atmosphere. PAMTRAM exploits the passive forward model to compute both
116 upward and downward looking polarized brightness temperatures and radiances; regarding radar measurements instead, the
117 active forward model yields Doppler spectra and relative moments, e.g. reflectivity, mean Doppler velocity, skewness, and
118 kurtosis. The model is built within a Fortran-Python environment, allowing the flexibility to different input/output formats and
119 instrument characteristics (e.g., observations from ground-based, airborne or spaceborne platforms, viewing angles, etc..), with
120 the assumption of a plane-parallel, one-dimensional homogeneous atmosphere over the horizontal direction. The user can
121 select several operational modes among scattering and absorption models, within a wide range of spectroscopic parameters
122 and databases; the absorption unit is based on the Millimeter-wave Propagation Model (MPM; Liebe, 1989). Generally,
123 pyPAMTRA is used in the scientific community, which features a Python wrapper built around the Fortran core, allowing
124 direct access from Python, without using the I/O Fortran routines. The pyPAMTRA interface makes the model user-friendly,
125 simplifying the importing of model data, the output in terms of files or plots, and the parallel running of the code on a multicore
126 processor or cluster machines.

127

128 **Py4CAAtS:** Python scripts for Computational Atmospheric Spectroscopy (Py4CAAtS, Schreier et al., 2019), is a software
129 designed for computing atmospheric spectroscopy both in the infrared and microwave spectral regions. It was initially
130 conceived to enable Python access to a previous Fortran 90 Generic Atmospheric Radiation Line-by-line Code (GARLIC,
131 Schreier et al., 2014). Later on, it has become a complete self-consistent independent software, based entirely on Python
132 numerical array processing modules, providing line by line radiances, as well as absorption cross sections and coefficients,
133 optical depths, transmissions and weighting functions. Py4CAAtS consists of a set of modules and functions allowing to
134 generate line-by-line cross sections for given pressure(s) and temperature(s), to combine cross sections into absorption
135 coefficients and optical depths, and to integrate along the line-of-sight into transmission and radiance/intensity. Py4CAAtS is
136 also user-friendly, since it offers an interactive environment and the possibility to perform batch line-by-line modeling. The
137 software can be started within the console terminal, the Python interpreter or the Jupyter Notebook; besides, all intermediate
138 variables can be visualized too. Py4CAAtS relies on a plane-parallel atmosphere assumption, and considers non-scattering
139 interactions, with the Schwarzschild equation featuring thermal emission as source only; furthermore, neither continuum nor
140 collision-induced absorptions are taken into account as contributions to the molecular absorption, which is therefore limited to
141 the Voigt Line shape.



142

143 **RTTOV**: Similar to CRTM, the Radiative Transfer for TOVS (RTTOV) is a fast radiative transfer model for modelling passive
144 visible, infrared and microwave downward-viewing satellite radiometers, spectrometers and interferometers (Saunders et al.,
145 2018; Hocking et al., 2021). RTTOV is a FORTRAN 90 code designed to be incorporated within user applications for
146 simulating satellite radiances. RTTOV is developed and maintained by the NWP Satellite Application Facility of EUMETSAT,
147 and it is probably the most used RT code for satellite data assimilation into NWP models. Given an atmospheric profile of
148 temperature, water vapour and, optionally, trace gases, aerosols and hydrometeors, together with surface parameters and a
149 viewing geometry, RTTOV computes the top of atmosphere radiances for a set of space-borne sensors from past, current, and
150 future satellite Earth observing missions. The core of RTTOV is a fast parameterisation of layer optical depths due to gas and
151 liquid water absorption. Profiles of layer-to-space transmittances computed by the line-by-line code AMSUTRAN (Turner et
152 al., 2019) are the basis for the training of the fast parameterisation. RTTOV consists in both the forward model, which simulates
153 the upwelling radiances for a given sensor, and its Jacobian, which calculates the radiance derivatives with respect to the input
154 atmospheric state variables. RTTOV includes scattering calculations for simulating cloudy and aerosol-affected radiances in
155 the infrared. Scattering at MW frequencies from hydrometeors of different phases and shapes is available through the wrapper
156 code RTTOV-SCAT (Bauer et al., 2010; Geer et al., 2017). RTTOV has a built-in graphic user interface (GUI) which allows
157 the user to modify an atmospheric/surface profile, run RTTOV for a given instrument, produce radiances and brightness
158 temperatures, calculate Jacobians, perform a basic retrieval, and display instantaneously the results. RTTOV is natively in
159 Fortran, but Python wrappers are available to allow the functionality of RTTOV in Python. These wrappers provide Python
160 bindings for the RTTOV Fortran code, making it easier for Python users to use. A ground-based version of RTTOV for
161 simulating ground-based MW sensors is also available, though limited to version 11 (De Angelis et al., 2016; Cimini et al.,
162 2019).

163

164 **TBUPDN**: The upward-downward T_b (TBUPDN) code is a library of Fortran routines for the non-scattering line-by-line
165 microwave RT simulations (Rosenkranz, 2017). The code is developed and maintained by Philip W. Rosenkranz since more
166 than 30 years (Rosenkranz, 1993). TBUPDN is intended as an educational tool with limited ranges of applicability, i.e.
167 calculations of upward- and downward-propagating T_b respectively at the top and bottom of the atmosphere. The main routines
168 can be run stand-alone or read as examples for using the subroutines (e.g., the absorption model routines) in other software
169 programs. A major feature of TBUPDN is the continuous update of absorption routines, originally based on the MPM code,
170 with subsequent spectroscopic modifications from most recent findings from laboratory and field campaign experiments
171 (Rosenkranz, 1988; 1998; 2001; 2005; Rosenkranz and Cimini, 2019; Gallucci et al., 2023). User interfaces are provided for
172 handling I/O text files and produce encapsulated postscript figures.

173

174 Table 1 and the list above are meant to provide an overview of open access codes that are used extensively by the MW
175 community, but do not pretend to be complete. Other codes suitable for atmospheric RT in the MW are available, either openly



176 or commercially, e.g., BTRAM (Chapman et al., 2010), MODTRAN (Berk et al., 2014). Other RT codes that are available in
177 Python or with a Python interface, although not concerning MW in Earth's atmosphere, include the following: PYDOME
178 (Efremenko et al. 2019) for simulating satellite measurements of reflected and scattered solar radiation in the ultraviolet and
179 visible spectral ranges; Py6S (Wilson, 2013), a Python interface to the 6S RTM (Vermote et al., 1997) designed to simulate
180 solar radiation through atmospheres on Earth and other planets; PySMARTS module (Ayala Pelaez and Deline, 2020) contains
181 functions for calling SMARTS: Simple Model of the Atmospheric Radiative Transfer of Sunshine to compute clear sky spectral
182 irradiances (on a tilted or horizontal receiver plane) for specified atmospheric conditions; petitRADTRANS (Mollière et al.,
183 2019) and PYRATE (Tritsis et al., 2018) for simulating RT through atmospheres on exoplanets.

184

185 This paper introduces PyRTlib, a new standalone Python package for non-scattering line-by-line microwave RT simulations.
186 Given the premises above, one may ask: is a new RT code really needed? The intention for PyRTlib is not to be considered a
187 competitor for the codes mentioned above, which represent the cutting edge with their own peculiarities, in terms of efficiency,
188 flexibility, modularity, and applicability. Nevertheless, the reasons behind the development of PyRTlib are the following:

- 189 1) Develop an educational tool, similarly to TBUPDN, but in Python, which represents nowadays the most used language
190 for scientific software development, especially by students and younger scientists;
- 191 2) Provide user-friendly Python interfaces, similarly to PyARTS or pyPAMTRA, to compute MW RT simulations using
192 popular datasets as input, such as radiosonde repository or global reanalysis;
- 193 3) Allow easy comparison of MW calculations using different atmospheric absorption models, e.g., those proposed
194 throughout the last three decades, for any platform (ground-based, airborne, and spaceborne) and observing geometry
195 (zenith, nadir, slant);
- 196 4) Provide T_B calculations with the associated uncertainty due to the uncertainty on spectroscopic parameters, following
197 a general rigorous approach recently outlined (Cimini et al., 2018; Gallucci et al., 2023).

198

199 In particular, to our knowledge the uncertainty estimate is not available by any other MW RT code, making PyRTlib unique
200 for this aspect in the MW RT scenario. Thus, this paper provides a description of PyRTlib version 1.0 and advocates its use
201 through a range of examples demonstrating its value in producing passive MW simulations from notable input datasets
202 (radiosondes, reanalysis) and for ground-based, airborne, and satellite perspectives.

203 The paper is structured as follows: brief introduction of the basics of equations of radiative transfer model, the main absorption
204 model available and how profiles can be interpolated and extrapolated are discussed in section 2. The tools for retrieving and
205 managing input data from open access repositories (e.g., radiosonde observations and model reanalysis) are discussed in
206 Section 3. Usage of the code as well as some implementation details and a few examples of applications are presented in
207 Section 4. Section 5 summarises the conclusions and future developments, while Section 6 provides instructions for code
208 availability and usage.



209 2 Radiative transfer model

210 An atmospheric RT model simulates the propagation of electromagnetic radiation through the atmosphere as it interacts with
211 the atmospheric constituents (gases, aerosols and hydrometers) through absorption, emission, scattering, and refraction. The
212 intensity of radiation I , also called radiance, expresses the power carried by the electromagnetic radiation along the direction
213 of propagation per unit area and solid angle at a given frequency f . Considering an ideal blackbody radiator in local
214 thermodynamic equilibrium at physical temperature T , the intensity of radiation I is given by the Planck function:

$$215 B_f(T) = \left(\frac{2hf^3}{c^2}\right) \left(\frac{1}{e^{hf/kT}-1}\right) \quad (1)$$

217 where h and k are the Planck and Boltzmann constants, respectively, and c is the speed of light. From Eq. (1) comes directly
218 the definition of brightness temperature T_B , as the temperature that a blackbody radiator should have to emit the radiance I ,
219 i.e., $I = B_f(T_B)$.

221 The relevance of radiation scattering by atmospheric particles depends on the ratio between the size of the scattering particle
222 r and the radiation wavelength λ , so called size ratio $x = 2\pi r/\lambda = 2\pi r f/c$ (Petty, 2006). If $x \ll 1$, then the contribution of
223 scattering can be considered negligible. That is the case at microwave and millimeter-wave frequencies ($\lesssim 1$ THz) in clear sky
224 (no clouds). For relatively small hydrometeors (i.e., liquid and ice clouds) the size ratio is still $x < 1$, and the Rayleigh
225 approximation is valid, for which absorption is still dominant with respect to scattering. Thus, a simplifying common
226 assumption at microwave frequencies is to neglect atmospheric scattering, which is commonly assumed valid in absence of
227 large particles (i.e., liquid and solid precipitation). In such a case, the Swartzchild equation applies, i.e.:

$$228 B_f(T_B) = B_f(T_{BG})e^{-\tau_f(0,\infty)} + \int_0^\infty B_f(T(s))\alpha_f(s)e^{-\tau_f(0,s)} ds \quad (2)$$

230 where s indicates the position along the propagation direction, α_f indicates the atmospheric absorption coefficient, τ_f indicates
231 the atmospheric opacity ($\tau_f(a,b) = \int_a^b \alpha_f(s)ds$), and the two extremes of the integral indicate the position where the T_B
232 measurement is taken (0) and the position of a uniform background (∞) of temperature T_{BG} . The first term of Eq.(2) changes
233 depending on the observing geometry. For an uplooking radiometer measuring downwelling radiation, without discrete sources
234 (such as the Sun or Moon) within the antenna field of view, $B_f(T_{BG})$ is simply equal to $B_f(T_{CBG})$, where $T_{CBG} \simeq 2.7$ K is the
235 microwave cosmic background brightness temperature (Rosenkranz, 1993). For a downlooking radiometer measuring
236 upwelling radiation, e.g. from a satellite platform, a typical background is the Earth's surface, the spectral emissivity (ϵ_f) of
237 which must be taken into account to model the complementary contribution of Earth's surface emission and reflection of
238



239 downwelling radiation. Thus, indicating with SRF the position of the Earth's surface and TOA the top of atmosphere, $B_f(T_{BG})$
 240 in Eq. (2) becomes:

241

$$242 \quad B_f(T_{BG}) = (1 - \varepsilon_f) \left[B_f(T_{CBG})e^{-\tau_f(SRF,TOA)} + \int_{SRF}^{TOA} B_f(T(s))\alpha_f(s)e^{-\tau_f(SRF,s)} ds \right] + \varepsilon_f B_f(T_{SRF}) \quad (3)$$

243

244 The integral in the atmospheric terms in Eq. (2) and (3) is divided into the sum of integrals over each of the NL-1 layers in
 245 between the NL levels in which the atmosphere is discretized (Schroeder and Westwater, 1991). In case of uplooking
 246 simulations of downwelling radiation:

247

$$248 \quad \int_0^{\infty} B_f(T(s))\alpha_f(s)e^{-\tau_f(0,s)} ds = \sum_{i=2}^{NL} \int_{s_{i-1}}^{s_i} B_f(T(s))\alpha_f(s)e^{-\tau_f(0,s)} ds \quad (4)$$

249

250 The integrals in the second term can be simplified by introducing a mean radiating temperature of a layer T_{MR} , such as:

251

$$252 \quad \int_{s_{i-1}}^{s_i} B_f(T(s))\alpha_f(s)e^{-\tau_f(0,s)} ds = B_f(T_{MR}) \int_{s_{i-1}}^{s_i} \alpha_f(s)e^{-\tau_f(0,s)} ds = B_f(T_{MR})e^{-\tau_f(0,s_{i+1})} [1 - e^{-\tau_f(s_{i+1},s_i)}] \quad (5)$$

253

254 $B_f(T_{MR})$ can be approximated as the weighted average of $B_f(T(s))$ from the two profile levels that form the layer:

255

$$256 \quad B_f(T_{MR}) \simeq \frac{B_f(T(s_{i-1})) + B_f(T(s_i))e^{-\tau_f(s_{i-1},s_i)}}{1 + e^{-\tau_f(s_{i-1},s_i)}} \quad (6)$$

257

258 where the exponential weight $e^{-\tau_f(s_{i-1},s_i)}$ represents the attenuation of $B_f(T(s_i))$ over the layer between levels i and $i-1$. The
 259 case of downlooking observations can be simply derived from the above. The contribution of each layer is then summed up as
 260 in Eq. (4) (Schroeder and Westwater, 1991).

261

262 2.1 Modelling atmospheric absorption

263 Modelling atmospheric absorption is a crucial component of RT codes. Absorption models are based on parameterized
 264 equations to calculate atmospheric absorption (α_f in Eq. (2)) given the constituents' concentration and their thermodynamic
 265 conditions (Rosenkranz, 1993). Note that, as introduced earlier, PyRtlib is a non-scattering RT code, i.e., it assumes that
 266 attenuation is due entirely to absorption by atmospheric gases and cloud water, while it neglects the extinction due to particle
 267 scattering. Concerning atmospheric gases, PyRtlib considers the absorption contribution by nitrogen and oxygen (also called
 268 dry air contribution, α_{dry}) and water vapour (wet contribution, α_{wet}). These three species sum up to more than 99% of the



269 atmospheric gas mixture and account for most of the gas absorption in the MW spectrum. PyRTlib also offers the option to
270 add the contribution of ozone (α_{O_3}); this causes a relatively small absorption increase in very narrow spectral ranges due to
271 many nearly monochromatic spectral lines at the expense of slower computations. Concerning hydrometeors, the absorption
272 of cloud liquid (α_{liq}) and ice (α_{ice}) particles are considered. Note that α_{dry} , α_{wet} , α_{O_3} , α_{liq} , and α_{ice} all depend on frequency
273 and location in space, although not shown for simplicity. In fact, the sum $\alpha_{dry} + \alpha_{wet} + \alpha_{O_3} + \alpha_{liq} + \alpha_{ice}$ represents $\alpha_f(s)$ in
274 Equations (2) and (3). Of course the terms α_{liq} and α_{ice} are zero in clear sky conditions while α_{O_3} is zero if ozone contribution
275 is neglected. Absorption models for computing α_{dry} , α_{wet} , α_{O_3} , α_{liq} , and α_{ice} from the constituents' concentration and the
276 thermodynamic conditions are available in the open literature (e.g., Rosenkranz, 1993). These models rely on parameterized
277 equations and spectroscopic parameters, valid up to 1 THz, determined through theoretical calculations and/or laboratory and
278 field measurements. These settings are continuously updated and improved (Liebe et al., 1989; Rosenkranz, 1998; Liljegren
279 et al., 2005; Turner et al., 2009; Mlawer et al., 2012; Koshelev et al., 2018). The proposed changes are occasionally summarised
280 in review articles (e.g., Rothman et al., 2005; Gordon et al., 2017, Rosenkranz, 1998; 2017; Tretyakov, 2016). In particular,
281 PyRTlib implements absorption routines originally based on the MPM code (Liebe, 1989), with subsequent spectroscopic
282 modifications from laboratory and field campaign experiments (Rosenkranz, 1988; 1998; 2005; 2015; 2017; Rosenkranz and
283 Cimini, 2019; Koshelev et al., 2021; 2022). These changes have been summarised in two papers (Cimini et al., 2018; Gallucci
284 et al., 2023). PyRTlib provides the possibility to easily compare different absorption model configurations, as discussed in one
285 of the examples in Section 4. In case the input profile contains non-zero cloud liquid and/or ice water, the relative absorption
286 is computed and added to the total absorption. The cloud absorption model used here assumes Rayleigh approximation, under
287 which scattering is negligible relative to absorption, and absorption is independent of cloud particle size distribution. These
288 assumptions restrict the model to non-precipitating clouds with particle radii less than about 100 μm for frequency less than
289 100 GHz. Therefore, in its current version, PyRTlib is not adequate for modelling extinction by rain or large cloud droplets
290 or ice particles. Absorption by cloud liquid (α_{liq}) and ice (α_{ice}) particles are implemented following the algorithms described
291 in Schroeder & Westwater (1991), and later improvements (i.e., Liebe et al., 1991; 1993). Optionally, a model designed
292 specifically for the absorption of supercooled liquid water particles (Rosenkranz, 2015) is also implemented.

293

294 **2.2 Modelling a continuous atmosphere**

295 To compute absorption throughout the atmosphere, the gas concentrations and thermodynamic profiles are to be provided in
296 input. While O_2 concentration is assumed constant with altitude, concentration of H_2O (and O_3 , if considered) is usually
297 variable with altitude, and similarly for air pressure and temperature. These inputs may come from atmospheric measurements
298 (e.g., balloon-borne radiosoundings) or atmospheric model output (e.g., NWP model), and are typically available at discrete
299 levels. To compute realistic simulated observations from ground-based or satellite platforms, the profiles must cover the
300 vertical range from the Earth surface to a reasonable top-of-atmosphere (TOA), where the atmosphere is so rare that it affects



301 MW radiation negligibly. In practice, the TOA is assumed to approximate the infinite limits on the integral in Eq.(2). For
302 simulations of downwelling radiation, the vertical range could be reduced at the bottom to the height of the simulated receiving
303 antenna (e.g., for the simulations of airborne or elevated instruments). PyRTlib provides functions to extend the input profile
304 to a TOA at 0.1 mb (following Schroeder and Westwater, 1991), a pressure well below the minimum pressure (i.e., maximum
305 altitude) reached by radiosoundings. This profile extension follows a recommendation (ITU-R P.835-6, 2017) by the
306 International Telecommunication Union - Radiocommunication Sector (ITU-R), providing expressions and data for reference
307 standard atmospheres required for the calculation of gaseous attenuation on Earth-space paths. In particular, PyRTlib currently
308 implements the data in Annex 1, i.e., standard atmospheres to be used to determine temperature, pressure and water-vapour
309 pressure as a function of altitude, when more reliable local data are not available. Data in Annex 3, i.e. providing vertical
310 profiles capturing diurnal, monthly, and seasonal variations from ECMWF 15-year data set re-analysis (ERA15) will be
311 implemented in future PyRTlib releases. Another option is to increase the level density by adding levels through interpolation.
312 This option allows a maximum pressure difference between a pair of adjacent profile levels. If the pressure difference in the
313 input profile exceeds the specified maximum value, PyRTlib divides the layer between the two levels into the smallest number
314 of equally-spaced pressure levels that differ by less than the specified maximum value, using linear interpolation in natural
315 logarithm of pressure.

316

317 2.3 Modelling observation geometry

318 The input height profile h is assumed to represent the vertical line-of-sight ray path coordinate. This corresponds to s in Eq.(2)
319 for uplooking zenith-pointing simulations and to h_{TOA-S} for downlooking nadir-pointing simulations. For observing angles
320 different from zenith or nadir, the ray path increases due to the slant path through the atmosphere. Considering a plane-parallel
321 atmosphere, the increase effectively corresponds to the multiplicative factor $secant\phi$, where ϕ is angle with respect to
322 zenith/nadir (or $cosecant\theta$, if the elevation angle θ is considered). This approximation is the default option in PyRTlib.
323 Atmospheric refraction can also be considered, which affects the ray path by radiation bending. Following Schroeder and
324 Westwater (1991), the ray path is modelled assuming a spherically stratified atmosphere for which the radio wave path obeys
325 Snell's law (Schroeder and Westwater, 1991):

326

$$327 \quad n r \cos\theta = constant \quad (7)$$

328

329 where n is the atmospheric refractive index and r is the radial distance from the center of the Earth to a point on the ray path.
330 All these qualities depend on height above the surface. The refractive index n is computed from the dry and wet refractivity
331 (N_d and N_w , respectively) and the inverse compressibility of dry air and water vapor (Z_d^{-1} and Z_w^{-1} , respectively) through the
332 following non-dispersive model:

333



$$334 \quad n = 1 + (N_d + N_w) \cdot 10^{-6} \quad (8)$$

$$335 \quad N_d = k_1 \left(\frac{P_d}{T} \right) Z_d^{-1} \quad (9)$$

$$336 \quad N_w = \left(k_2 \frac{e}{T} + k_3 \frac{e}{T^2} \right) Z_w^{-1} \quad (10)$$

$$337 \quad Z_d^{-1} = 1 + P_d \left(57.90 \cdot 10^{-8} \left(1 + \frac{0.52}{T} \right) - 9.4611 \cdot 10^{-4} \frac{T-273.16}{T^2} \right) \quad (11)$$

$$338 \quad Z_w^{-1} = 1 + 1650 \frac{e}{T^3} (1 - 0.01317 T_c + 1.75 \cdot 10^{-4} T_c^2 + 1.44 \cdot 10^{-6} T_c^3) \quad (12)$$

339

340 where T , e , P_d are respectively the air temperature (K), water vapour partial pressure, and dry air partial pressure (hPa), while
341 T_c is the air temperature in °C ($T_c = T - 273.16$). The three k coefficients ($k_1 = 77.604$, $k_2 = 64.79$, $k_3 = 3.776 \cdot 10^5$) are
342 given by Saastamoinen, 1972 and references therein. PyRTlib optionally provides a slightly modified definition for computing
343 the dry and wet refractivity terms, though leaving the total refractivity and the refractive index unaffected, which is commonly
344 used in geodesy (ESA TN, 2019). Finally, for each specified observing angle a ray-tracing algorithm based on Eq.(7) is used
345 to compute the refracted path length between each pair of adjacent profile levels. The integrals along the ray path are computed
346 assuming that the integrand variable decays exponentially with height within the layer defined by a pair of adjacent levels.
347 With this assumption, the integral along one layer of a general integrand variable X is given by (Schroeder and Westwater,
348 1991):

349

$$350 \quad \int_{s_{i-1}}^i X(s) ds = (s_i - s_{i-1}) [(X(s_i) - X(s_{i-1})) / \ln(X(s_i)/X(s_{i-1}))] \quad (13)$$

351

352 This is used to compute path-integrated quantities, such as layer-integrated absorption profiles for RT calculations as well as
353 total integrals along the entire path, such as precipitable water vapour, path delay (excess path length) due to dry air and to
354 water vapour, and total absorption due to water vapour, dry air, and cloud liquid/ice.

355 **3 Tools for retrieving input data**

356 PyRTlib comes with a built-in module to easily retrieve meteorological data that can be used as input for the RT calculations.
357 These modules allow easy access to data repositories of radiosonde observations (RAOB) and model reanalysis. The RAOB
358 repositories currently considered in PyRTlib are the University of Wyoming Upper Air Archive (UWYO, 2015) and the U.S.
359 National Center for Environmental Information (NCEI) Integrated Radiosonde Archive (IGRA) version 2 (Durre et al., 2016).
360 These datasets are retrieved by using part of the Siphon (<https://github.com/Unidata/siphon>) library from UNIDATA.
361 Concerning model reanalysis, PyRTlib currently considers the ECMWF 5th-generation Reanalysis (ERA5) as accessible from
362 the Climate Data Store Application Program Interface (CDS API) (<https://github.com/ecmwf/cdsapi>) service. The following
363 subsections describe how the above datasets can be accessed through PyRTlib.



364 3.1 Radiosondes

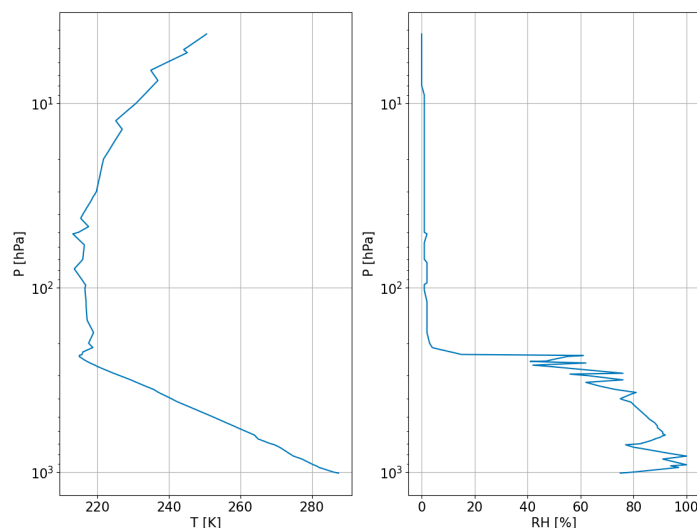
365 Balloon-borne measurements from radiosondes provide high resolution accurate profiles of temperature, humidity and wind
366 from the altitude of the launching site up to the altitude where the balloon bursts (~ 30 km for a successful launch). This
367 information is an important piece of the global observing system, and it is widely used in atmospheric research and related
368 services, such as operational meteorology, air quality forecast, climatology, NWP validation and data assimilation, and finally
369 the calibration and validation of remote sensing observations. The Wyoming Upper Air Archive from the University of
370 Wyoming consists of radiosonde balloons from more than 628 globally distributed stations over the world. The data are
371 available at synoptic hours (00-06-12-18 UTC) starting from 1973. The available variables are latitude, longitude and elevation
372 of each launching station, and the atmospheric profiles of pressure, geopotential height, temperature, dew point temperature,
373 frost point temperature, relative humidity, relative humidity with respect to ice, water vapour mixing ratio, wind direction,
374 wind speed, potential temperature, equivalent potential temperature, and virtual potential temperature. The vertical resolution
375 varies from tens of meters in the lower layers to hundreds of meters near the tropopause, changing according to the site and
376 weather conditions. Listing 1 shows the code to retrieve and plot data measured by one radiosonde launched at 12 UTC 22
377 April 2021 from the station named LIRE (Pratica di Mare, Italy), leading to the graphic output in Figure 1. Data from any other
378 station available on the Wyoming Upper Air Archive can be accessed knowing the station name or number that can be found
379 through their web interface (<https://weather.uwyo.edu/upperair/sounding.html>).

```
import matplotlib.pyplot as plt
from datetime import datetime

from pyrtlib.apiwebservices import WyomingUpperAir
from pyrtlib.utils import to_kelvin
from datetime import datetime

date = datetime(2021, 4, 22, 12)
station = 'LIRE'
df = WyomingUpperAir.request_data(date, station)
df.temperature = to_kelvin(df.temperature)
df.plot("temperature", 'pressure',
        xlabel="T [K]", ylabel="P [hPa]",
        grid=True, legend=False)
df.plot("rh", 'pressure',
        xlabel="RH [%]", ylabel="P [hPa]",
        grid=True, legend=False)
plt.gca().invert_yaxis()
plt.yscale('log')
```

380 **Listing 1.** Example code using PyRTlib module to retrieve radiosonde data from the Wyoming Upper Air archive.



381
382 **Figure 1.** Graphical output of Listing 1, showing atmospheric profiles measured by the radiosonde launched at 12:00 UTC on
383 22 April 2021 from the LIRE station (Pratica di Mare, Italy). Left: Temperature profile (K). Right: Relative Humidity (%).
384

385 Another well known repository for radiosonde data is the Integrated Global Radiosonde Archive (IGRA), consisting of
386 radiosonde and pilot balloon observations from more than 2800 stations distributed globally. The earliest data dates back to
387 1905 and recent data becomes available in near real time from around 800 stations all over the world. The recording period,
388 temporal and vertical resolution for each station vary over time. Observations are available at standard and variable pressure
389 levels, fixed and variable height wind levels, surface and tropopause. Variables include time since launch and profiles of
390 atmospheric pressure, temperature, geopotential height, dew point depression, wind direction and speed at a variable number
391 of levels, including surface, tropopause, mandatory standard and optional significant levels. The data are released after a quality
392 assurance algorithm performed by the archiving system, checking for format problems, physically implausible values, internal
393 inconsistencies among variables, climatological outliers, and temporal and vertical inconsistencies (Durre et al., 2016; 2018).
394 The IGRA is accessible through NCEI, which also provides access to IGRA station metadata, including information about
395 changes in the station's location, instrumentation, and observation practices over time, that may be useful for interpreting the
396 data. Listing 2 shows the code to retrieve and plot data measured by one radiosonde launched at 12 UTC 22 June 2022 from
397 the station network-id SPM00060018 (Tenerife, Spain), leading to the graphic output in Figure 2. Data from any other station
398 available on IGRA can be accessed knowing the station network-id that can be found through their web interface
399 (<https://www.ncei.noaa.gov/data/integrated-global-radiosonde-archive/doc/igra2-station-list.txt>). Note that PyRTlib provides
400 tools to convert atmospheric moisture variables to the standard input relative humidity (e.g., in the given example, the function
401 dewpoint2rh computes relative humidity from dew point depression and physical temperature). PyRTlib then internally
402 computes water vapour pressure and density from temperature and relative humidity using the Goff-Gratch formulas for



403 saturation vapour pressure over liquid and ice water, according to a user-specified switch that determines whether the saturation
404 vapour pressure is calculated over water throughout the profile or over ice when temperature is below a given threshold.

```
from pyrtlib.apiwebservices import IGRAUpperAir
from pyrtlib.utils import to_kelvin, dewpoint2rh
from datetime import datetime

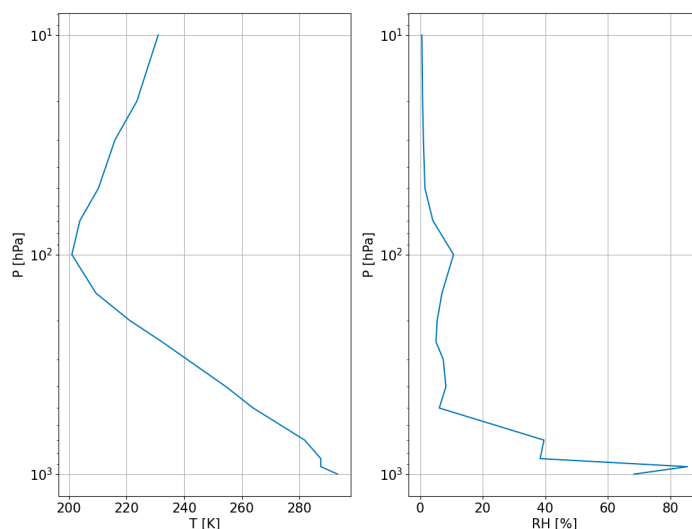
date = datetime(2022, 6, 22, 12)
station = 'SPM00060018'
df, header = IGRAUpperAir.request_data(date, station)
df = df[df.pressure.notna() &
        df.temperature.notna() &
        df.dewpoint.notna() &
        df.height.notna()]

rh = dewpoint2rh(df.dewpoint, df.temperature).values
df.relative_humidity = rh * 100
df.temperature = to_kelvin(df.temperature)

df.plot("temperature", 'pressure',
        xlabel="T [K]", ylabel="P [hPa]",
        grid=True, legend=False)
df.plot("relative_humidity", 'pressure',
        xlabel="RH [%]", ylabel="P [hPa]",
        grid=True, legend=False)

plt.gca().invert_yaxis()
plt.yscale('log')
```

405 **Listing 2.** Example code using PyRTlib module to retrieve radiosonde data from the IGRA2 archive.



406
407 **Figure 2.** Graphical output of Listing 2, showing atmospheric profiles measured by the radiosonde launched at 12:00 UTC on
408 22 June 2022 from the station SPM00060018 (Tenerife, Spain). Left: Temperature profile (K). Right: Relative Humidity (%).



409 3.2 Model reanalysis

410 Model reanalysis is an optimal combination of past observations with atmospheric models to provide the most accurate
411 representation of the status of the atmosphere at sub-daily intervals on a regular 3D spatial grid. In short, forecast models and
412 4D data assimilation systems are used periodically to “reanalyse” archived observations based on variational optimal
413 estimation method. Model reanalysis has substantially evolved during recent decades in generating a consistent time series of
414 multiple climate variables, and are nowadays among the most-used datasets in geophysical sciences. ERA5 is the fifth and
415 latest generation of global climate reanalysis produced by ECMWF, providing hourly data of many atmospheric, land-surface
416 and sea-state parameters together with estimates of uncertainty. ERA5 is based on the most recent and advanced version of the
417 ECMWF Integrated Forecasting System (IFS) model and significantly improved compared to its predecessors (Hersbach et
418 al., 2020). ERA5 is produced and continuously updated by the Copernicus Climate Change Service (C3S) and made available
419 through the Climate Data Store (CDS). ERA5 data are archived on a reduced Gaussian grid, which has quasi-uniform spacing
420 over the globe, at native resolution of 0.28125 degrees (31 km), from the surface up to about 80 km height. Data can be
421 accessed in either GRIB (native) or NetCDF format. PyRTlib implements data retrieval in NetCDF format, which is
422 automatically converted and interpolated from the native grids to a regular latitude/longitude grid ($0.125^\circ \times 0.125^\circ$ grid, i.e.
423 ~ 16 km at the equator) at 37 pressure levels. Hourly estimates of a large number of gridded atmospheric, land and oceanic
424 climate variables are included from 1979 onwards, with a 5-day delay from real time. Among the available variables the
425 following are selected as input for PyRTlib: temperature, relative humidity, specific cloud ice water content, specific cloud
426 liquid water content, ozone mass mixing ratio. Listing 3 shows the code to retrieve ERA5 data from the Copernicus CDS for
427 the nearest grid point to a location in Southern Italy (longitude 16.04°; latitude 39.44°) on 16 May 2023 at 18:00 UTC. Listing
428 3 also shows tools to convert the native units for cloud water variables (mass mixing ratios, kg/kg) in liquid and ice water
429 density (g/m^3), and plots cloud liquid water content (CLWC), cloud ice water content (CIWC), and ozone mass mixing ratio
430 (Figure 3). Data from any other location worldwide from 1979 onwards with a 5-day delay from real time can be accessed by
431 simply providing longitude, latitude, date and hour. Note that to access the ERA5 dataset requires configuring an API key.
432 Step-by-step instructions to create an API key are available at: <https://cds.climate.copernicus.eu/api-how-to>.

```
import tempfile
from pyrtlib.apiwebservices import ERA5Reanalysis
from pyrtlib.utils import kgkg_to_kgm3

lonlat = (16.04, 39.44)
date = datetime(2023, 5, 16, 18)
nc_file = ERA5Reanalysis.request_data(tempfile.gettempdir(), date, lonlat)

df_era5 = ERA5Reanalysis.read_data(nc_file, lonlat)

total_mass = 1 - df_era5.ciwc.values - df_era5.clwc.values - df_era5.crcw.values - df_era5.cswc.values
denice = df_era5.ciwc.values * (1/total_mass) * \
    kgkg_to_kgm3(df_era5.q.values * (1/total_mass),
                df_era5.p.values, df_era5.t.values) * 1000
denliq = df_era5.clwc.values * (1/total_mass) * \
    kgkg_to_kgm3(df_era5.q.values * (1/total_mass),
```



```
df_era5.p.values, df_era5.t.values) * 1000

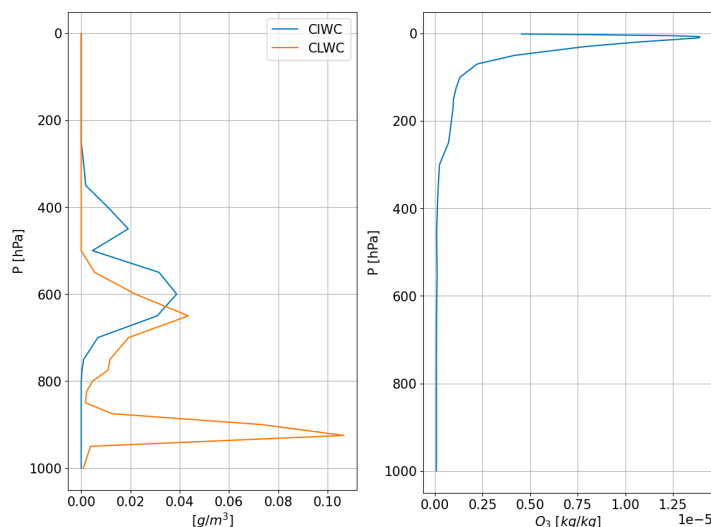
df_era5['denice'] = denice
df_era5['denliq'] = denliq

plt.plot(df_era5.denice, df_era5.p, label='CIWC')
plt.plot(df_era5.denliq, df_era5.p, label='CLWC')
plt.xlabel("[g/m^3]")
plt.ylabel("P [hPa]")
plt.gca().invert_yaxis()
plt.legend()
plt.grid()

df_era5.plot("o3", 'p',
            xlabel="$O_3$ [kg/kg]", ylabel="P [hPa]",
            grid=True, legend=False)

plt.gca().invert_yaxis()
```

433 **Listing 3.** Example code using PyRTLlib module to retrieve atmospheric profiles from the ERA5 Reanalysis.



434 **Figure 3.** Graphical output of Listing 3, showing atmospheric profiles from ERA5 reanalysis for the nearest grid point to a
435 location in Southern Italy (longitude 16.04°; latitude 39.44°) on 16 May 2023 at 18:00 UTC. Left: Cloud liquid water content
436 (CLWC) and cloud ice water content (CIWC). Right: ozone mass mixing ratio.
437

438 4 Examples of applications

439 PyRTLlib was developed to provide an educational RT software in Python, especially targeting students and younger scientists
440 that mostly use this language for scientific code development. For this reason, PyRTLlib was built with additional modules for
441 facilitating the retrieval and management of popular datasets as input, such as radiosonde repository or global reanalysis, as
442 shown in Section 3. This makes PyRTLlib a useful end-to-end RT tool for pedagogical purposes, being flexible and interactive
443 with easy access to all kinds of intermediate variables (e.g., absorption, optical depth, opacity, mean radiating temperature). In



444 addition, PyRTLlib was designed to allow easy comparison of MW RT calculations using a set of atmospheric absorption models
445 proposed throughout the last three decades, for any platform (ground-based, airborne, and spaceborne) and observing geometry
446 (zenith, nadir, slant). Finally, PyRTLlib implements a general rigorous approach to estimate the uncertainty related to the
447 absorption model (Cimini et al., 2018; Gallucci et al., 2023) and thus it provides T_B calculations with the associated uncertainty
448 estimate, to our knowledge a unique feature in the MW RT scenario. In the following, few examples of applications are given,
449 together with the output figure and the simple code for obtaining it.

450 4.1 Simulation of downwelling T_B

451 As a first example, we propose the simulation of downwelling T_B spectra in a typical MW spectral range. This simple example
452 may turn useful to simulate the measurements from a multi-channel ground-based microwave radiometer, e.g. those widely
453 deployed in atmospheric profiling observatories (Rüfenacht et al., 2021; Shrestha et al., 2022). As input, the user can opt for
454 one of the six climatological atmospheric profiles predefined in PyRTLlib (from Anderson et al., 1986: TROPICAL, MIDLAT
455 WINTER, MIDLAT SUMMER, ARCTIC WINTER, ARCTIC SUMMER, US STANDARD) or any of the
456 radiosonde/reanalysis profiles retrieved from the repositories introduced in Section 3. Listing 4 shows the code to compute
457 and plot downwelling T_B spectra at 1-GHz frequency resolution for two typical climatology conditions (tropical and subarctic
458 winter), each at two pointing angles (90° and 30° elevation angle). The graphic output, reported in Figure 4, shows the typical
459 peaks corresponding to resonant absorption of atmospheric gases (O_2 at 50-70 and 118 GHz, H_2O at 22.2 and 183 GHz) as
460 well as the non-resonant continuum absorption due to H_2O (monotonically increasing with frequency). The peaks and the
461 continuum show the emission added by the atmospheric gases with respect to the relatively cold emission coming from the
462 outer boundary of the atmosphere (the so called cosmic background). T_B spectra are generally higher for tropical conditions,
463 due to higher atmospheric temperature and humidity with respect to subarctic winter, and for lower elevation angles, due to
464 the slant longer path travelled by radiation throughout the atmosphere.

```
from pyrtlib.tb_spectrum import TbCloudRTE
from pyrtlib.climatology import AtmosphericProfiles as atmp
from pyrtlib.utils import ppmv2gkg, mr2rh

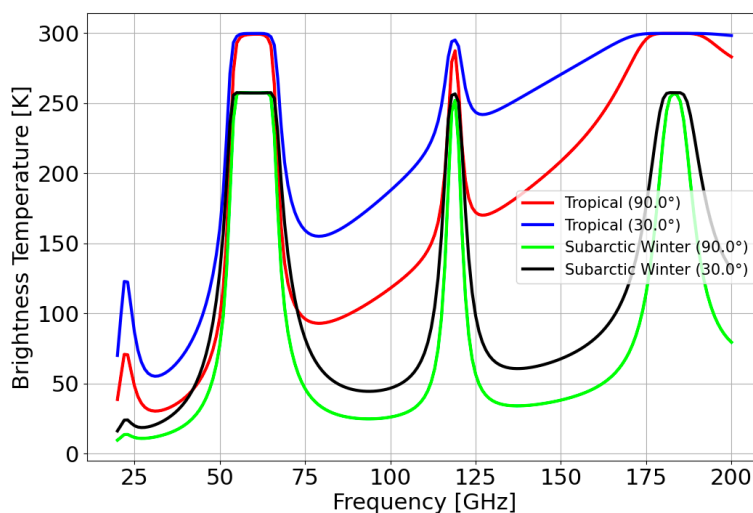
colors = ['#ff0405', '#0404ff', '#0fff0e', '#000000']
atms = [atmp.TROPICAL, atmp.SUBARCTIC_WINTER]
cnt = 0
for atm in atms:
    z, p, _, t, md = atmp.g1_atm(atm)
    gkg = ppmv2gkg(md[:, atmp.H20], atmp.H20)
    rh = mr2rh(p, t, gkg)[0] / 100
    frq = np.arange(20, 201, 1)
    ang = np.array([90., 30.])

    for a in ang:
        rte = TbCloudRTE(z, p, t, rh, frq, np.array([a]))
        rte.init_absmdl('R19SD')
        rte.satellite = False
        df = rte.execute()
        df = df.set_index(frq)
```



```
df.tbtotal.plot(figsize=(12,8), xlabel="Frequency [GHz]", ylabel="Brightness Temperature [K]",  
                label=atmp.atm_profiles()[atm] + ' (' + str(a) + '°)', lw=3, legend=True,  
                color=colors[cnt], grid=True)  
cnt += 1
```

465 **Listing 4.** Example code using PyRTlib module to calculate downwelling T_B in the 20 to 201 GHz spectral range (1 GHz
466 resolution) using two predefined climatological profiles (Tropical and Subarctic Winter) at 90° and 30° elevation angle.



467 **Figure 4.** Graphical output of Listing 4, showing downwelling T_B spectra computed for two typical climatologies (Tropical
468 and Subarctic Winter) at two elevation angles (90° and 30°).
469

470 4.2 Simulation of upwelling T_B

471 The second example shows the simulation of upwelling T_B spectra, as those typically sampled by satellite-based MW
472 radiometers (e.g., Moradi et al., 2015). Listing 5 shows the code to compute and plot upwelling T_B spectra at 1-GHz frequency
473 resolution for typical mid-latitude summer climatology conditions. The graphic output, reported in Figure 5, shows that the
474 strong emission features (e.g., at 60-70, 118, 183 GHz) appear flipped with respect to Section 4.1, indicating gas absorption
475 that removes radiation from the emission coming from the relatively warm background Earth's surface. The impact of pointing
476 angle and surface emissivity are shown by varying their values. In particular, 90° pointing angle indicates nadir observations,
477 while 37° indicates typical observing angle of MW imagers (53° from nadir), while 0.9 and 0.45 represent typical high and
478 low emissivity values in the MW spectral region. PyRTlib also allows frequency-dependent surface emissivity to be provided
479 in input.

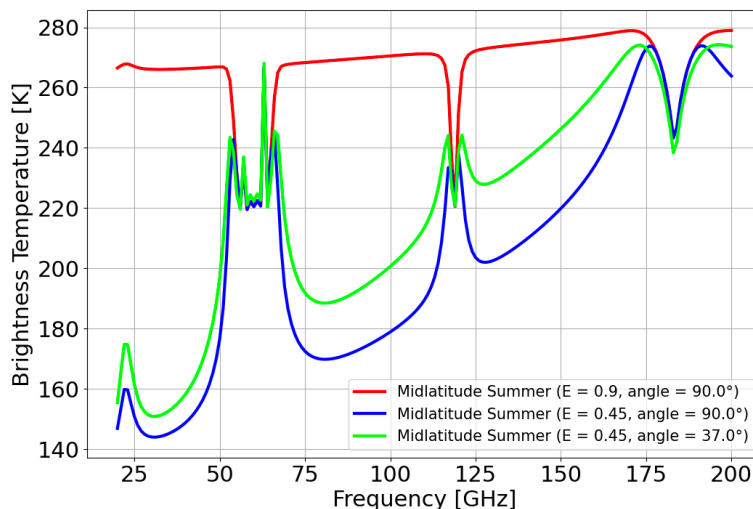
```
from pyrtlib.tb_spectrum import TbCloudRTE  
from pyrtlib.climatology import AtmosphericProfiles as atmp  
from pyrtlib.utils import ppmv2gkg, mr2rh  
  
z, p, _, t, md = atmp.gl_atm(atmp.MIDLATITUDE_SUMMER)  
gkg = ppmv2gkg(md[:, atmp.H2O], atmp.H2O)  
rh = mr2rh(p, t, gkg)[0] / 100
```



```
frq = np.arange(20, 201, 1)
ang = np.array([90., 37.])

colors = ['#ff0405', '#0404ff', '#0fff0e']
cnt = 0
for a in ang:
    rte = TbCloudRTE(z, p, t, rh, frq, np.array([a]))
    rte.init_absmdl('R19SD')
    for e in [0.9, 0.45]:
        if a == 37. and e == 0.90:
            continue
        rte.emissivity = e
        df = rte.execute()
        df = df.set_index(frq)
        df.tbtotal.plot(figsize=(12,8), xlabel="Frequency [GHz]", ylabel="Brightness Temperature [K]",
                        label=atmp.atm_profiles()[atmp.MIDLATITUDE_SUMMER] + ' (E = ' + str(e) + ', angle = ' +
str(a) + '°)',
                        color=colors[cnt], lw=3, legend=True, grid=True)
        cnt += 1
```

480 **Listing 5.** Example code using PyRTlib module to calculate upwelling T_B in the 20 to 201 GHz spectral range (1 GHz
481 resolution) using a predefined climatological profile (Midlatitude Summer) at 90° and 37° elevation angle with constant surface
482 emissivity at 0.9 and 0.45.



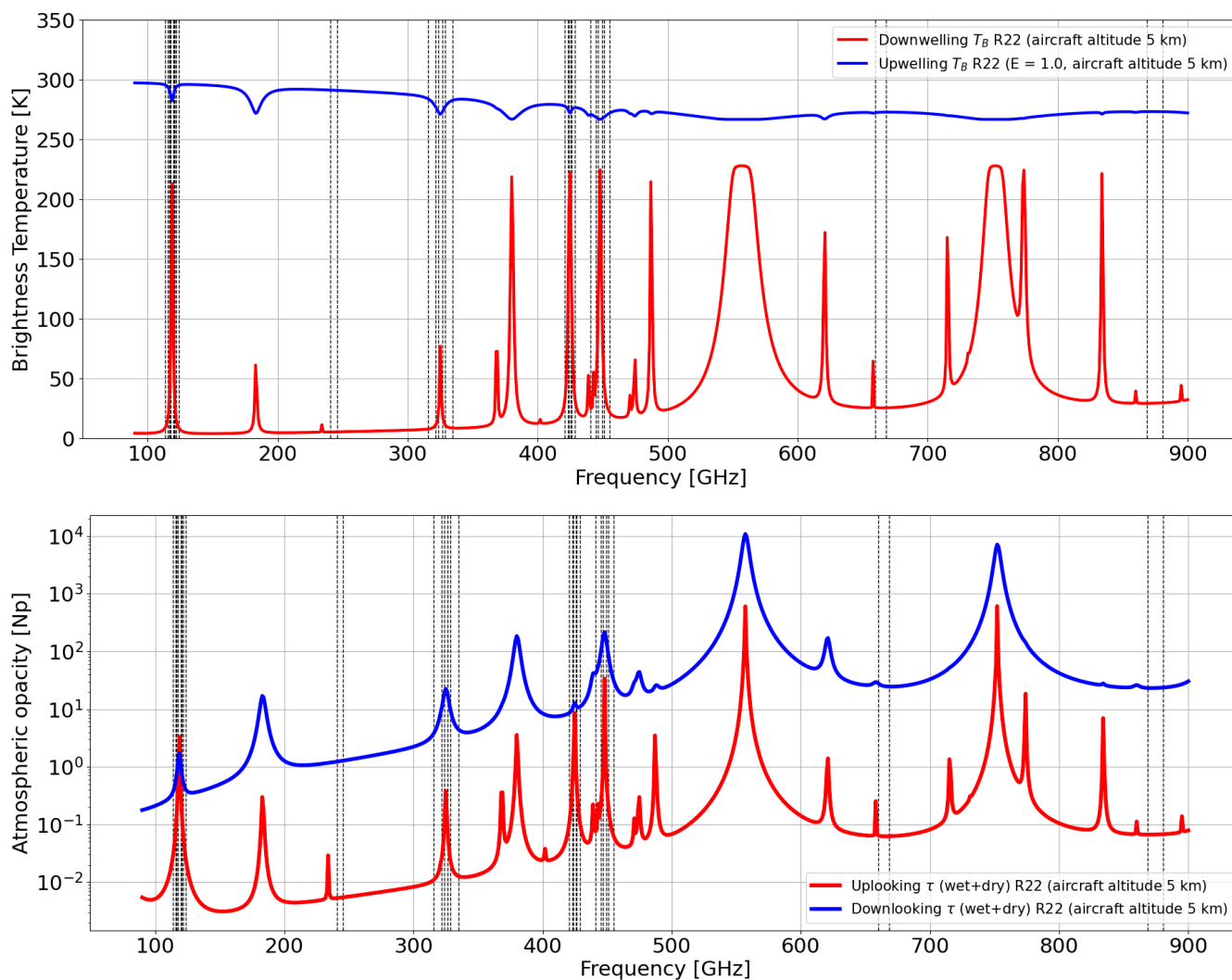
483 **Figure 5.** Graphical output of Listing 5, showing upwelling T_B spectra computed for a predefined climatological profile
484 (Midlatitude Summer) at 90° and 37° elevation angle with constant surface emissivity at 0.9 and 0.45.
485

486 4.3 Simulation of simultaneous downwelling and upwelling T_B

487 Simultaneous observations of downwelling and upwelling T_B are typically performed from airborne scanning instruments that
488 can alternate uplooking and downlooking views (e.g., Fox et al., 2017; Wang et al., 2017). Both views can be simulated by
489 PyRTlib using the same atmospheric profile in input and specifying the altitude of the aircraft and the observing angle. Figure
490 6 shows the downwelling and upwelling T_B simulated assuming the aircraft at 5 km altitude looking down at nadir and up at



491 zenith. The input profile comes from a radiosonde launched from Camborne (UK) at 12:00 UTC on 22 July 2021 and retrieved
492 from the Wyoming Upper Air Archive, corresponding to location and period of experimental flights by the Facility for
493 Airborne Atmospheric Measurements (FAAM) BAe-146 aircraft mounting the International Submillimetre Airborne
494 Radiometer (ISMAR, Fox et al., 2017). ISMAR has 17 channels spanning the 118 to 874 GHz range, being developed as an
495 airborne demonstrator for the Ice Cloud Imager (ICI), planned for the second generation of European polar-orbiting satellites
496 (MetOp-SG) to be launched 2024 onwards. Note that PyRTLlib functions allow to display and investigate not only T_B but all
497 the intermediate RT variables, such as absorption, optical depth, opacity. For example, Figure 6 shows the atmospheric opacity
498 above and below the aircraft as computed for the uplooking and downlooking views.



499

500

501 **Figure 6.** Top: downwelling and upwelling T_B simulating aircraft observations at respectively zenith and nadir from 5 km
502 altitude (gas absorption model: R22; surface emissivity equal to 1). Bottom: Atmospheric opacity computed for the uplooking



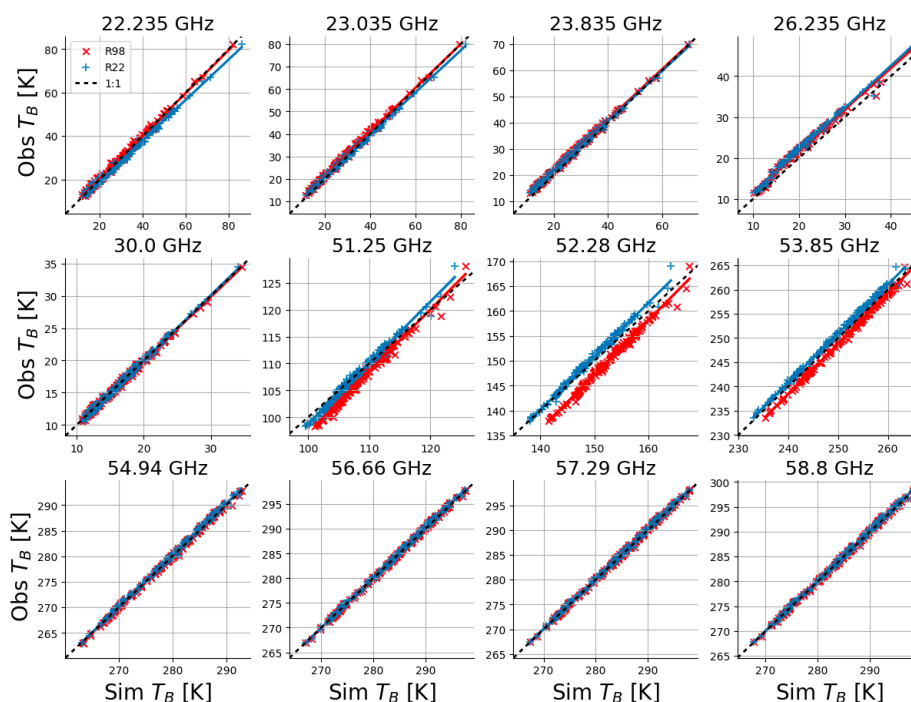
503 and downlooking views. Input profile from the radiosonde launched from Camborne (UK) on 22 July 2021 at 12:00 UTC and
504 retrieved from the Wyoming Upper Air Archive. Vertical black lines indicate the ISMAR channel frequencies.

505 **4.4 Comparison of absorption models**

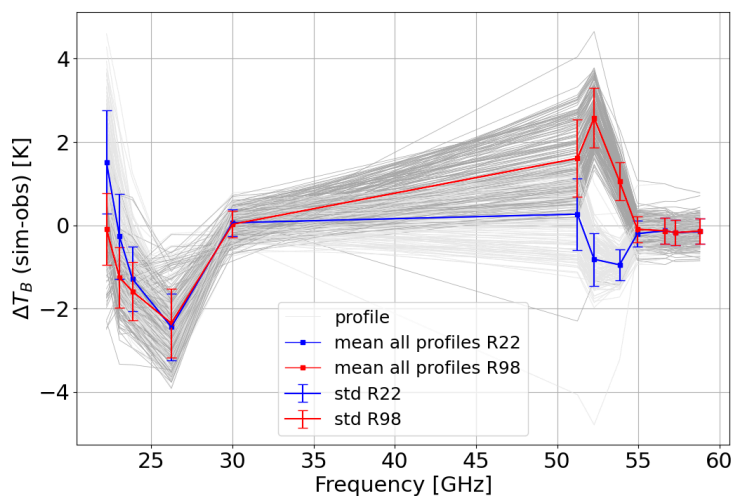
506 The PyRTlib package allows T_B simulations with different versions of atmospheric gas absorption models. As mentioned
507 earlier, the spectroscopy underlying absorption models is continuously updated, following the latest findings from laboratory
508 and field campaign experiments. Currently, PyRTlib implements absorption routines originally based on the MPM code (Liebe,
509 1989) with spectroscopy modified throughout the last decades. Specifically, the following versions are readily callable in
510 PyRTlib (with reference to the paper that motivated the update, where available): R98 (Rosenkranz, 1998); R03 (Tretyakov et
511 al., 2003), R16, R17 (Rosenkranz, 2017), R19, R19SD (Rosenkranz and Cimini, 2019), R20, R20SD (Makarov et al., 2020),
512 R21SD (Koshelev et al., 2021), until R22SD (Koshelev et al., 2022). The original Fortran code for most of these absorption
513 routines by P. W. Rosenkranz are freely accessible through a repository (http://cetemps.aquila.infn.it/mwrnet/lblmrt_ns.html).
514 In the following, we present an example in which the latest version at the time of writing, R22SD, is compared with R98,
515 which still represents a widely used model (e.g., Picard et al., 2009). Modifications in R22SD with respect to R98 include:
516 updated line width at 22 GHz (Payne et al., 2008), updated water vapor continuum coefficients scaled after Turner et al. (2009),
517 revised O_2 mixing coefficients for 50-70 GHz and 118 GHz lines (Makarov et al., 2020), speed-dependent line shape for the
518 water vapor absorption lines at 22 (Rosenkranz and Cimini, 2019) and 183 GHz (Koshelev et al., 2021), addition of four
519 submillimeter wave water vapor lines (860, 970, 987, 1097 GHz), and other updated line parameters taken from the most
520 recent release of the HITRAN database (HITRAN2020). To test two gas absorption versions, a simple observation minus
521 simulation (O-S) approach can be used, exploiting MW ground-based remote sensing and balloon-borne sounding
522 measurements from the US Department of Energy (DOE) Atmospheric Radiation Measurement (ARM) program
523 (<https://arm.gov>), which can be freely accessed from the ARM data center (<https://adc.arm.gov>). In fact, ARM deploys a
524 network of ground-based MW radiometers (MWR) across its observatory sites (Cadeddu et al., 2013; Cadeddu & Liljegren,
525 2018). These instruments measure downwelling T_B at selected frequency channels under all-sky conditions. From the same
526 sites, ARM regularly launches radiosondes; the ARM balloon-borne sounding system (BBSS) products provide profiles of in
527 situ measurements of atmospheric pressure, temperature, humidity, as well as wind speed and direction (Holdridge, 2020),
528 which can be given in input to PyRTlib to simulate zenith downwelling T_B . A dataset of colocated and nearly simultaneous
529 MWR observations and RT simulations can be then used to test and validate simulations from different absorption models.
530 Such a dataset was retrieved from the deployment of the ARM mobile facility in Highland Center, Cape Cod (MA, USA)
531 during the two-column aerosol project (TCAP) in 2012 (Titos et al., 2014). The observations are the T_B measured by a MWR
532 profiler (MWRP). The MWRP product provides measurements of T_B at 12 frequency channels in the range from 22 to 58 GHz.
533 Frequencies between 22 and 52 GHz are mostly sensitive to atmospheric water vapor and cloud liquid, while frequencies
534 between 51 and 60 GHz are sensitive to atmospheric temperature through the absorption of atmospheric oxygen. Simulations
535 at the same frequency channels are computed from the 4-daily radiosondes (at 05:30, 11:30, 17:30, and 23:30 UTC) launched



536 during TCAP and processed by PyRTLlib. To avoid spatial-temporal uncertainty of clouds, the comparison is made in clear-sky
537 conditions, applying a cloud screening to both radiosonde and MWRP data. Clear-sky conditions were selected using a relative
538 humidity threshold, specifically rejecting radiosondes with at least four pressure levels with relative humidity higher than 95%
539 (Clain et al., 2015). Furthermore, an observation-based screening was applied, removing data for which 1-h standard deviation
540 of the T_B at 30 GHz was larger than 0.5 K, indicating possible obstructions or cloud contamination (De Angelis et al., 2017).
541 From a total of 592 radiosonde, these two screenings leave 149 match-ups for the analysis. Simulated and observed datasets
542 were compared by selecting and averaging MWRP observations falling within -45 minute/ $+1$ hour from each radiosonde
543 launch time, so as to reduce the temporal-spatial mismatch with respect to the radiosonde measurements. The result of the
544 comparison of R98 and R22 models versus the observed dataset is shown in Figure 7 and 8.



545
546 **Figure 7.** Scatter plots of downwelling T_B as observed by a MWRP (y-axis) and simulated with PyRTLlib (x-axis) using two
547 versions of the gas absorption model (R98 in red x and R22 in blue +). Each panel shows one MWRP channel. Markers show
548 153 MWRP-radiosonde match-ups in clear sky selected from a 6-month period during the TCAP campaign. MWRP and
549 radiosonde data were retrieved from the ARM data center (Cadeddu and Gibler, 2012; Keeler and Burk, 2012).
550



551

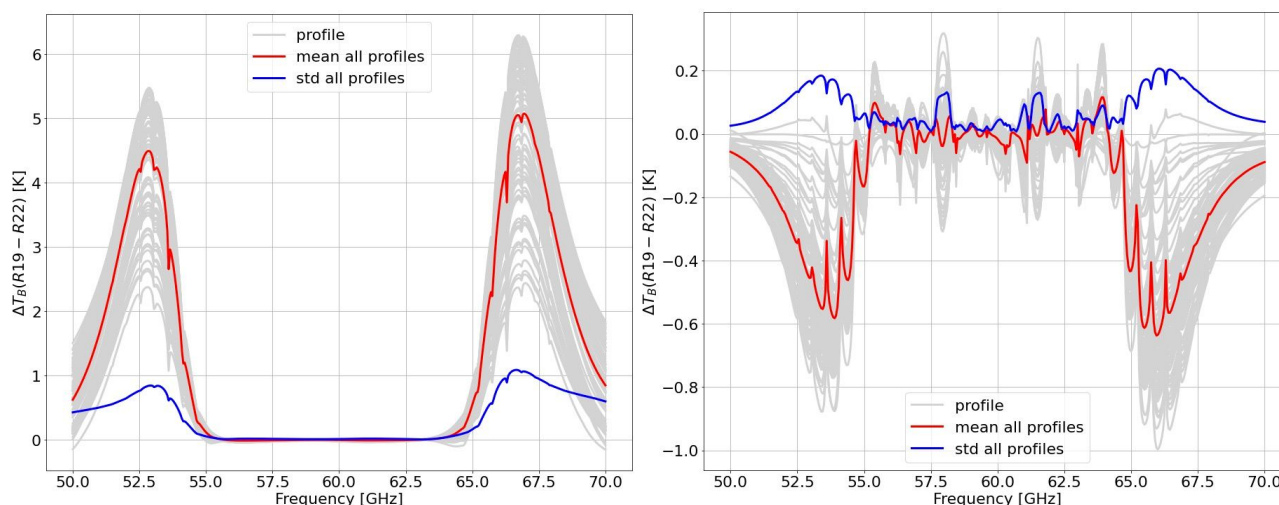
552 **Figure 8.** Spectrum of simulations minus observations statistics from the 153 MWRP-radiosonde match-ups in clear sky
553 dataset in Figure 7. Simulations computed using R98 are shown in red, while using R22 in blue. Dots and bars indicate
554 respectively the mean value and the standard deviation over the whole dataset.

555

556 Figure 7 clearly shows that RT simulations with both absorption models follow nicely observed T_B over the whole range of
557 variations for all MWRP channels, although larger differences are evident at 51–54 GHz for R98. Bias of the same order of
558 magnitude for the 51–54 GHz channels were previously reported for the R98 model employing MWR of different types and
559 manufacturers (e.g., Löhnert and Maier, 2012; De Angelis et al., 2017). De Angelis et al. (2017) attribute these to a combination
560 of systematic uncertainties stemming from inaccurate instrument bandpass characterization, instrument calibration, and
561 absorption model. Since then, two major updates have been proposed for the O_2 spectroscopic parameters in this range (mainly
562 mixing coefficients) from laboratory experiments (Tretyakov et al., 2005; Makarov et al., 2020), the latest of which is
563 implemented in R22. Figure 8 reports mean and standard deviation of the simulation minus observation differences, which
564 indicate better performances for R22 with respect to R98 in modelling T_B for channels along the low-frequency wing of the
565 O_2 absorption complex, confirming recent independent results (Belikovich et al., 2021; 2022). Unexpectedly, Figure 8 also
566 indicates differences ~ 2 K for R22 at 22.2 and 26.235 GHz channels, which will be discussed in next Section. PyRTlib also
567 allows quantifying the impact on T_B of the most recent set of O_2 spectroscopic parameters (Makarov et al., 2020) with respect
568 to the previous one (Tretyakov et al., 2005). In fact, two absorption model versions implemented in PyRTlib, namely R19
569 and R22, only differ by this aspect in the 50–70 GHz range, and thus the T_B impact is simply evaluated by computing T_B with
570 these two versions and taking the difference. To make it general, we evaluate the impact by processing the set of 83 diverse
571 atmospheric profiles commonly used to train RTTOV (Saunders et al, 2018). This profile set was carefully chosen from more
572 than 100 million profiles to represent a realistic range of possible diverse atmospheric conditions (Matricardi, 2008) and it is
573 openly available through the Numerical Weather Prediction Satellite Application Facility (NWPSAF) ([https://nwp-
574 saf.eumetsat.int/site/software/atmospheric-profile-data/](https://nwp-saf.eumetsat.int/site/software/atmospheric-profile-data/)). Figure 9 shows the differences between the two models for the



575 downwelling and upwelling T_B simulated at 50 MHz resolution from the 83 diverse profiles, together with the mean difference
576 and standard deviation (std). For downwelling T_B , the updated O_2 mixing coefficients proposed by Makarov et al. (2020)
577 decrease T_B with respect to the previous ones (Tretyakov et al., 2005) by up to 4-5 K on average, peaking at 53 and 66 GHz,
578 with an estimated global variability ~ 1 K (1-sigma). For upwelling T_B , the situation is opposite, with a decrease up to -0.6 K
579 with 0.2 K std, although it depends on the assumed surface emissivity (set to 1 in this example).



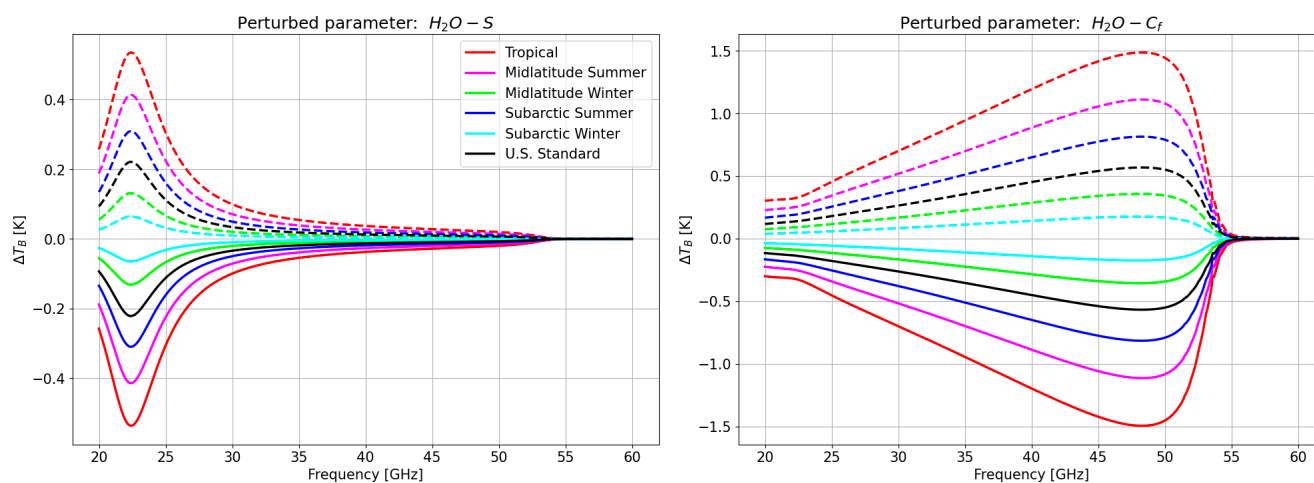
580
581 **Figure 9.** Differences of downwelling (left) and upwelling (right) T_B computed with R19 and R22 absorption models at 50
582 MHz resolution for the set of NWPSAF 83 diverse profiles. Red and blue lines indicate mean difference and standard deviation
583 of the dataset. Upwelling simulations assume constant surface emissivity equal to 1.

584 4.5 Absorption model uncertainty

585 RT calculations depend on absorption models and the underlying spectroscopic parameters. The values of these parameters
586 are determined through theoretical assumptions or analysis of laboratory or field data, and thus are inherently affected by
587 uncertainty. The uncertainty affecting the spectroscopic parameters contributes to the uncertainty of the absorption, which
588 affects the RT calculations, and in turn the retrieval of atmospheric variables from remotely sensed observations (Cimini et al.,
589 2018). PyRTlib allows to compute the sensitivity of RT calculations to the uncertainty of various spectroscopic parameters,
590 defined as the T_B difference (ΔT_B) obtained by perturbing the value of spectroscopic parameter by its uncertainty. Figure 10
591 reports the sensitivity of zenith downwelling T_B to two water vapor absorption spectroscopic parameters, namely the line
592 intensity (S) at 22.2 GHz and the foreign continuum coefficient (C_f), showing consistency with results in Cimini et al. (2018,
593 Figure 2). In addition to the uncertainty of individual parameters, the correlation between the uncertainty on various parameters
594 must also be taken into account, and therefore it is necessary to calculate the complete uncertainty covariance matrix
595 (Rosenkranz, 2005). A general and rigorous approach to estimate the uncertainty covariance matrix for MW absorption models
596 has been outlined (Rosenkranz et al., 2018) and applied to the simulations of downwelling (Cimini et al., 2018) and upwelling

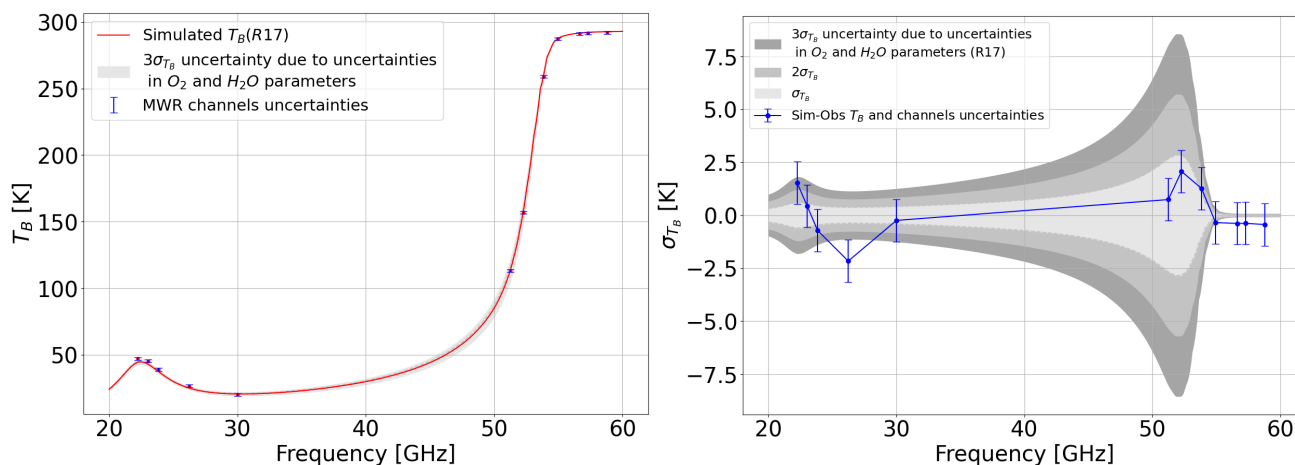


597 (Gallucci et al., 2023) radiation. PyRTLlib inherits this development and provides tools to compute T_B together with the
598 associated uncertainty estimate. One example is shown in Figure 11. Here, zenith downwelling T_B is computed from one
599 radiosonde from the TCAP dataset, together with the associated uncertainty estimate $\sigma(T_B)$ and compared with the nearly
600 simultaneous measurements from the colocated MWRP with its typical calibration uncertainty (Cadeddu & Liljegren, 2018).
601 Figure 11 shows that for this single case the observation minus simulation differences fit within the overlap of instrumental
602 calibration uncertainty and absorption model uncertainty at 3-sigma, and for some channels, at 1-sigma level. The only channel
603 that is nearly off is the 26.235 GHz. This happens also for other radiosondes and absorption models, as evident in Figure 8,
604 suggesting that the calibration of this particular channel is questionable and may need recalibration service.



605
606 **Figure 10.** Sensitivity of zenith downwelling T_B to water vapor absorption parameters, computed at 0.1 GHz spectral
607 resolution. Left: line intensity (S) at 22 GHz. Right: foreign continuum coefficient (C_f). Solid lines correspond to negative
608 perturbation (value - uncertainty), while dashed lines correspond to positive perturbation (value + uncertainty). Different
609 colors indicate six typical climatological conditions. Adapted from Cimini et al., 2018.

610



611
612 **Figure 11.** Left: Zenith downwelling T_B spectrum (red line) computed from one radiosonde launched from the ARM mobile
613 facility during TCAP, Cape Cod, MA, USA (2012-08-26 16:58 UTC). Blue points and bars indicate the nearly simultaneous
614 measurements from the colocated MWRP at 12 frequency channels and their calibration uncertainty. Right: Simulations minus
615 observations at the 12 channels (blue points) with the instrumental calibration uncertainty (blue bars), together with the
616 estimated uncertainty for zenith downwelling T_B ($\sigma(T_B)$) due to the uncertainty in absorption model spectroscopic parameters
617 (at 1-, 2-, and 3-sigma levels).

618 5 Summary and future developments

619 This paper presents PyRTlib, a Python library for non-scattering atmospheric microwave radiative transfer computations. The
620 intention for PyRTlib is to provide a user-friendly tool for computing down and up-welling brightness temperatures and related
621 quantities (e.g., atmospheric absorption, optical depth, opacity) in Python, a flexible language that nowadays represents the
622 most used for scientific software development, especially by students and early career scientists. Within its limits, mainly non
623 scattering and 1-D geometry, PyRTlib allows simulating observations from ground-based, airborne, and satellite microwave
624 sensors in clear sky and in cloudy conditions (under Rayleigh approximation). Clearly, the intention for PyRTlib is not to be
625 a competitor for other radiative transfer codes that excel for computational efficiency (RTTOV, CRTM), flexibility (ARTS),
626 modularity (ARTS, Py4CATS), and applicability (ARTS, PAMTRA). Nevertheless, despite the speed limitations and the
627 omission of important aspects of RT (e.g., spherical geometry and particle scattering), we believe PyRTlib is attractive as an
628 educational tool because of the flexibility and ease of use, providing a quick interface to popular repositories of atmospheric
629 profiles from radiosondes and model reanalysis. PyRTlib also allows peculiar investigations such as absorption model
630 comparison and validation against observations (e.g., Section 4.4) and the estimation of brightness temperature uncertainty
631 due to atmospheric absorption model (e.g., Section 4.5). In addition, PyRTlib could be used as a module for other Python codes
632 that need atmospheric radiative transfer, e.g. the Snow Microwave Radiative Transfer model (SMRT, Picard et al. 2018).
633 Future developments include the implementation of (*i*) new absorption models (e.g. R23 came out at the time of submission),



634 (ii) sensor-oriented calculations considering channels' spectral response functions, (iii) uncertainty estimate for higher
635 frequency brightness temperature calculations, as recently investigated (Gallucci et al., 2023), (iv) additional tools for
636 extrapolating the input profiles (e.g., Annex 3 of ITU-R P.835-6), (v) additional tools for accessing other atmospheric data
637 open repositories to be used as RT calculations input, e.g., the ARM data center and the Global Climate Observing System
638 Reference Upper Air Network (GRUAN, Bodeker et al., 2016).

639 **6 Code and data availability**

640 PyRTlib is available as a python package to users under an open-source GPL v3 license and it is free of charge. PyRTlib may
641 be obtained from the github repository <https://github.com/SatCloP/pyrtlib> or from the Zenodo repository
642 <https://doi.org/10.5281/zenodo.8219145>. Instructions for installing and running PyRTlib are provided in the PyRTlib User
643 Guide Documentation available at <https://satclop.github.io/pyrtlib>. The user documentation is rich in content and includes a
644 large number of examples on how to run and configure PyRTlib. The python package also includes scripts and test suite to
645 verify the installation and Jupyter Notebook examples for running the PyRTlib modules to be easily performed in your work
646 environment. PyRTlib is designed for multiplatform systems (UNIX/Linux, MacOS, Windows) and can be installed on any
647 computer supporting Python3.6 (or higher) to work properly.

648 **7 Competing interests**

649 The contact author has declared that none of the authors has any competing interests.

650 **8 Acknowledgements**

651 The authors acknowledge the support of EUMETSAT through the ISMAR study (contract EUM/CO/20/4600002477/VM) and
652 the VICIRS study (contract EUM/CO/22/4600002714/FDA). The authors also acknowledge the support of ESA through the
653 REFDAT4ESAMWR project (contract 4000134771/21/NL/MG/mkn). PyRTlib development was also stimulated through the
654 COST Action CA18235 PROBE, supported by COST (European Cooperation in Science and Technology,
655 <https://www.cost.eu/>). The authors acknowledge the advice of Phil W. Rosenkranz (MIT, retired) and Stuart Fox (MetOffice)
656 throughout the software development.

657
658 *Author contributions.* SL, DC, and DG designed the research, contributed to data processing and analysis, and wrote the
659 original manuscript. SL and DC developed the software with support from all co-authors. FR contributed to validation data
660 analysis. All the co-authors helped to revise the manuscript.

661



662 **References**

- 663 Anderson, G. P., Clough, S. A., Kneizys, F. X., Chetwynd, J. H., and Shettle, E. P.: AFGL atmospheric constituent
664 profiles (0.120km), Unknown, 1986.
- 665 Anon: University of Wyoming Upper Air Archive, n.d.
- 666 Ayala Pelaez, S. and Deline, C.: pySMARTS: SMARTS Python Wrapper (Simple Model of the Atmospheric
667 Radiative Transfer of Sunshine), , <https://doi.org/10.11578/DC.20210816.1>, 2020.
- 668 Bauer, P., Geer, A. J., Lopez, P., and Salmond, D.: Direct 4D-Var assimilation of all-sky radiances. Part I:
669 Implementation, Quarterly Journal of the Royal Meteorological Society, 136, 1868–1885,
670 <https://doi.org/10.1002/qj.659>, 2010.
- 671 Belikovich, M. V., Kulikov, M. Y., Makarov, D. S., Skalyga, N. K., Ryskin, V. G., Shvetsov, A. A., Krasil'nikov,
672 A. A., Dementyeva, S. O., Serov, E. A., and Feigin, A. M.: Long-Term Observations of Microwave Brightness
673 Temperatures over a Metropolitan Area: Comparison of Radiometric Data and Spectra Simulated with the Use of
674 Radiosonde Measurements, Remote Sensing, 13, 2061, <https://doi.org/10.3390/rs13112061>, 2021.
- 675 Belikovich, M. V., Makarov, D. S., Serov, E. A., Kulikov, M. Y., and Feigin, A. M.: Validation of Atmospheric
676 Absorption Models within the 20–60 GHz Band by Simultaneous Radiosonde and Microwave Observations: The
677 Advantage of Using ECS Formalism, Remote Sensing, 14, 6042, <https://doi.org/10.3390/rs14236042>, 2022.
- 678 Berk, A., Conforti, P., Kennett, R., Perkins, T., Hawes, F., and Bosch, J. van den: MODTRAN6: a major upgrade
679 of the MODTRAN radiative transfer code, in: Algorithms and Technologies for Multispectral, Hyperspectral, and
680 Ultraspectral Imagery XX, Algorithms and Technologies for Multispectral, Hyperspectral, and Ultraspectral
681 Imagery XX, 113–119, <https://doi.org/10.1117/12.2050433>, 2014.
- 682 Bodeker, G. E., Bojinski, S., Cimini, D., Dirksen, R. J., Haeffelin, M., Hannigan, J. W., Hurst, D. F., Leblanc, T.,
683 Madonna, F., Maturilli, M., Mikalsen, A. C., Philipona, R., Reale, T., Seidel, D. J., Tan, D. G. H., Thorne, P. W.,
684 Vömel, H., and Wang, J.: Reference Upper-Air Observations for Climate: From Concept to Reality, Bulletin of the
685 American Meteorological Society, 97, 123–135, <https://doi.org/10.1175/BAMS-D-14-00072.1>, 2016.
- 686 Boukabara, S.-A., Garrett, K., Grassotti, C., Iturbide-Sanchez, F., Chen, W., Jiang, Z., Clough, S. A., Zhan, X.,
687 Liang, P., Liu, Q., Islam, T., Zubko, V., and Mims, A.: A physical approach for a simultaneous retrieval of
688 sounding, surface, hydrometeor, and cryospheric parameters from SNPP/ATMS, Journal of Geophysical Research:
689 Atmospheres, 118, 12,600–12,619, <https://doi.org/10.1002/2013JD020448>, 2013.
- 690 Buehler, S. A., Eriksson, P., Kuhn, T., von Engeln, A., and Verdes, C.: ARTS, the atmospheric radiative transfer
691 simulator, Journal of Quantitative Spectroscopy and Radiative Transfer, 91, 65–93,
692 <https://doi.org/10.1016/j.jqsrt.2004.05.051>, 2005.
- 693 Buehler, S. A., Defer, E., Evans, F., Eliasson, S., Mendrok, J., Eriksson, P., Lee, C., Jiménez, C., Prigent, C.,
694 Crewell, S., Kasai, Y., Bennartz, R., and Gasiewski, A. J.: Observing ice clouds in the submillimeter spectral range:



- 695 the CloudIce mission proposal for ESA's Earth Explorer 8, *Atmospheric Measurement Techniques*, 5, 1529–1549,
696 <https://doi.org/10.5194/amt-5-1529-2012>, 2012.
- 697 Buehler, S. A., Mendrok, J., Eriksson, P., Perrin, A., Larsson, R., and Lemke, O.: ARTS, the Atmospheric Radiative
698 Transfer Simulator – version 2.2, the planetary toolbox edition, *Geoscientific Model Development*, 11, 1537–1556,
699 <https://doi.org/10.5194/gmd-11-1537-2018>, 2018.
- 700 Cadeddu, M. and Gibler, G.: Microwave Radiometer Profiler (MWRP), <https://doi.org/10.5439/1025254>, 2012.
- 701 Cadeddu, M. P. and Liljegren, J.: Microwave Radiometer Profiler (MWRP) Instrument Handbook,
702 <https://doi.org/10.2172/1424403>, 2018.
- 703 Cadeddu, M. P., Payne, V. H., Clough, S. A., Cady-Pereira, K., and Liljegren, J. C.: Effect of the Oxygen Line-
704 Parameter Modeling on Temperature and Humidity Retrievals From Ground-Based Microwave Radiometers, *IEEE*
705 *Transactions on Geoscience and Remote Sensing*, 45, 2216–2223, <https://doi.org/10.1109/TGRS.2007.894063>,
706 2007.
- 707 Cadeddu, M. P., Liljegren, J. C., and Turner, D. D.: The Atmospheric radiation measurement (ARM) program
708 network of microwave radiometers: instrumentation, data, and retrievals, *Atmospheric Measurement Techniques*,
709 6, 2359–2372, <https://doi.org/10.5194/amt-6-2359-2013>, 2013.
- 710 Chapman, I. M., Naylor, D., Gom, B. G., Querel, R. R., and Davis-Imhof, P.: BTRAM : An Interactive Atmospheric
711 Radiative Transfer Model, 2010.
- 712 Cimini, D., Rosenkranz, P. W., Tretyakov, M. Y., Koshelev, M. A., and Romano, F.: Uncertainty of atmospheric
713 microwave absorption model: impact on ground-based radiometer simulations and retrievals, *Atmospheric*
714 *Chemistry and Physics*, 18, 15231–15259, <https://doi.org/10.5194/acp-18-15231-2018>, 2018.
- 715 Cimini, D., Hocking, J., Angelis, F. D., Cersosimo, A., Paola, F. D., Gallucci, D., Gentile, S., Gerdali, E., Larosa,
716 S., Nilo, S., Romano, F., Ricciardelli, E., Ripepi, E., Viggiano, M., Luini, L., Riva, C., Marzano, F. S., Martinet,
717 P., Song, Y. Y., Ahn, M. H., and Rosenkranz, P. W.: RTTOV-gb v1.0 – updates on sensors, absorption models,
718 uncertainty, and availability, *Geoscientific Model Development*, 12, 1833–1845, <https://doi.org/10.5194/gmd-12-1833-2019>, 2019.
- 720 Cimini, D., Serio, C., Masiello, G., Mastro, P., Ricciardelli, E., Paola, F. D., Larosa, S., Gallucci, D., Hultberg, T.,
721 August, T., and Romano, F.: Spectrum Synergy for Investigating Cloud Microphysics, *Bulletin of the American*
722 *Meteorological Society*, 104, E606–E622, <https://doi.org/10.1175/BAMS-D-22-0008.1>, 2023.
- 723 Clain, G., Brogniez, H., Payne, V. H., John, V. O., and Luo, M.: An Assessment of SAPHIR Calibration Using
724 Quality Tropical Soundings, *Journal of Atmospheric and Oceanic Technology*, 32, 61–78,
725 <https://doi.org/10.1175/JTECH-D-14-00054.1>, 2015.



- 726 Clough, S. A., Shephard, M. W., Mlawer, E. J., Delamere, J. S., Iacono, M. J., Cady-Pereira, K., Boukabara, S.,
727 and Brown, P. D.: Atmospheric radiative transfer modeling: a summary of the AER codes, *Journal of Quantitative*
728 *Spectroscopy and Radiative Transfer*, 91, 233–244, <https://doi.org/10.1016/j.jqsrt.2004.05.058>, 2005.
- 729 De Angelis, F., Cimini, D., Hocking, J., Martinet, P., and Kneifel, S.: RTTOV-gb – adapting the fast radiative
730 transfer model RTTOV for the assimilation of ground-based microwave radiometer observations, *Geoscientific*
731 *Model Development*, 9, 2721–2739, <https://doi.org/10.5194/gmd-9-2721-2016>, 2016.
- 732 De Angelis, F., Cimini, D., Löhnert, U., Caumont, O., Haefele, A., Pospichal, B., Martinet, P., Navas-Guzmán, F.,
733 Klein-Baltink, H., Dupont, J.-C., and Hocking, J.: Long-term observations minus background monitoring of
734 ground-based brightness temperatures from a microwave radiometer network, *Atmospheric Measurement*
735 *Techniques*, 10, 3947–3961, <https://doi.org/10.5194/amt-10-3947-2017>, 2017.
- 736 Ding, S., Yang, P., Weng, F., Liu, Q., Han, Y., van Delst, P., Li, J., and Baum, B.: Validation of the community
737 radiative transfer model, *Journal of Quantitative Spectroscopy and Radiative Transfer*, 112, 1050–1064,
738 <https://doi.org/10.1016/j.jqsrt.2010.11.009>, 2011.
- 739 Durre, I., Yin, X., Vose, R. S., Applequist, S., Arnfield, J., Korzeniewski, B., and Hundermark, B.: Integrated
740 Global Radiosonde Archive (IGRA), Version 2, <https://doi.org/10.7289/V5X63K0Q>, 2016.
- 741 Durre, I., Yin, X., Vose, R. S., Applequist, S., and Arnfield, J.: Enhancing the Data Coverage in the Integrated
742 Global Radiosonde Archive, *Journal of Atmospheric and Oceanic Technology*, 35, 1753–1770,
743 <https://doi.org/10.1175/JTECH-D-17-0223.1>, 2018.
- 744 Efremenko, D. S., Molina García, V., Pflug, B., and Trautmann, T.: PYDOME: python library for radiative transfer
745 computations, in: *Living Planet Symposium 2019*, 2019.
- 746 Eriksson, P., Jiménez, C., and Buehler, S. A.: Qpack, a general tool for instrument simulation and retrieval work,
747 *Journal of Quantitative Spectroscopy and Radiative Transfer*, 91, 47–64,
748 <https://doi.org/10.1016/j.jqsrt.2004.05.050>, 2005.
- 749 Eriksson, P., Buehler, S. A., Davis, C. P., Emde, C., and Lemke, O.: ARTS, the atmospheric radiative transfer
750 simulator, version 2, *Journal of Quantitative Spectroscopy and Radiative Transfer*, 112, 1551–1558,
751 <https://doi.org/10.1016/j.jqsrt.2011.03.001>, 2011.
- 752 ESA TN TEC-EEP/2016.184/AM, Tropospheric Media Calibration System for accurate ranging of space science
753 missions - Definitions of parameters and test procedures for assessment of instrument stability, ver 2.5, November
754 2019.
- 755 Eyre, J. R., English, S. J., and Forsythe, M.: Assimilation of satellite data in numerical weather prediction. Part I:
756 The early years, *Quarterly Journal of the Royal Meteorological Society*, 146, 49–68,
757 <https://doi.org/10.1002/qj.3654>, 2020.



- 758 Fox, S., Lee, C., Moyna, B., Philipp, M., Rule, I., Rogers, S., King, R., Oldfield, M., Rea, S., Henry, M., Wang,
759 H., and Harlow, R. C.: ISMAR: an airborne submillimetre radiometer, *Atmospheric Measurement Techniques*, 10,
760 477–490, <https://doi.org/10.5194/amt-10-477-2017>, 2017.
- 761 Gallucci D., D. Cimini, S. Fox, E. Turner, P. Rosenkranz, M. Tretyakov, V. Mattioli, and F. Romano: Uncertainty
762 of simulated brightness temperature due to sensitivity to atmospheric gas spectroscopic parameters, (work in
763 preparation), 2023
- 764 Geer, A. J., Baordo, F., Bormann, N., Chambon, P., English, S. J., Kazumori, M., Lawrence, H., Lean, P., Lonitz,
765 K., and Lupu, C.: The growing impact of satellite observations sensitive to humidity, cloud and precipitation,
766 *Quarterly Journal of the Royal Meteorological Society*, 143, 3189–3206, <https://doi.org/10.1002/qj.3172>, 2017.
- 767 Gordon, I. E., Rothman, L. S., Hill, C., Kochanov, R. V., Tan, Y., Bernath, P. F., Birk, M., Boudon, V., Campargue,
768 A., Chance, K. V., Drouin, B. J., Flaud, J.-M., Gamache, R. R., Hodges, J. T., Jacquemart, D., Perevalov, V. I.,
769 Perrin, A., Shine, K. P., Smith, M.-A. H., Tennyson, J., Toon, G. C., Tran, H., Tyuterev, V. G., Barbe, A., Császár,
770 A. G., Devi, V. M., Furtenbacher, T., Harrison, J. J., Hartmann, J.-M., Jolly, A., Johnson, T. J., Karman, T., Kleiner,
771 I., Kyuberis, A. A., Loos, J., Lyulin, O. M., Massie, S. T., Mikhailenko, S. N., Moazzen-Ahmadi, N., Müller, H. S.
772 P., Naumenko, O. V., Nikitin, A. V., Polyansky, O. L., Rey, M., Rotger, M., Sharpe, S. W., Sung, K., Starikova,
773 E., Tashkun, S. A., Auwera, J. V., Wagner, G., Wilzewski, J., Wcisło, P., Yu, S., and Zak, E. J.: The HITRAN2016
774 molecular spectroscopic database, *Journal of Quantitative Spectroscopy and Radiative Transfer*, 203, 3–69,
775 <https://doi.org/10.1016/j.jqsrt.2017.06.038>, 2017.
- 776 Han, Y., van Delst, P., Liu, Q., Weng, F., Yan, B., Treadon, R., and Derber, J.: JCSDA Community Radiative
777 Transfer Model (CRTM) : version 1, 2006.
- 778 Hersbach, H., Bell, B., Berrisford, P., Hirahara, S., Horányi, A., Muñoz-Sabater, J., Nicolas, J., Peubey, C., Radu,
779 R., Schepers, D., Simmons, A., Soci, C., Abdalla, S., Abellan, X., Balsamo, G., Bechtold, P., Biavati, G., Bidlot,
780 J., Bonavita, M., De Chiara, G., Dahlgren, P., Dee, D., Diamantakis, M., Dragani, R., Flemming, J., Forbes, R.,
781 Fuentes, M., Geer, A., Haimberger, L., Healy, S., Hogan, R. J., Hólm, E., Janisková, M., Keeley, S., Laloyaux, P.,
782 Lopez, P., Lupu, C., Radnoti, G., de Rosnay, P., Rozum, I., Vamborg, F., Villaume, S., and Thépaut, J.-N.: The
783 ERA5 global reanalysis, *Quarterly Journal of the Royal Meteorological Society*, 146, 1999–2049,
784 <https://doi.org/10.1002/qj.3803>, 2020.
- 785 Hocking, J., Vidot, J., Brunel, P., Roquet, P., Silveira, B., Turner, E., and Lupu, C.: A new gas absorption optical
786 depth parameterisation for RTTOV version 13, *Geoscientific Model Development*, 14, 2899–2915,
787 <https://doi.org/10.5194/gmd-14-2899-2021>, 2021.
- 788 Holdridge, D.: Balloon-Borne Sounding System (SONDE) Instrument Handbook, Atmospheric Radiation
789 Measurement user facility, Pacific Northwest National Laboratory, Richland, WA,
790 <https://doi.org/10.2172/1020712>, 2020.



- 791 ITU-R Recommendation P.835-6, Reference standard atmospheres, available at [https://www.itu.int/rec/R-REC-](https://www.itu.int/rec/R-REC-P.835/en)
792 [P.835/en](https://www.itu.int/rec/R-REC-P.835/en), Last accessed: 26 July 2021, approved December 2017.
- 793 Karpowicz, B. M., Stegmann, P. G., Johnson, B. T., Christophersen, H. W., Hyer, E. J., Lambert, A., and Simon,
794 E.: pyCRTM: A python interface for the community radiative transfer model, *Journal of Quantitative Spectroscopy*
795 *and Radiative Transfer*, 288, 108263, <https://doi.org/10.1016/j.jqsrt.2022.108263>, 2022.
- 796 Keeler, E. and Burk, K.: Balloon-Borne Sounding System (SONDEWNP), <https://doi.org/10.5439/1595321>,
797 2012.
- 798 Koshelev, M. A., Golubiatnikov, G. Yu., Vilkov, I. N., and Tretyakov, M. Yu.: Line shape parameters of the 22-
799 GHz water line for accurate modeling in atmospheric applications, *Journal of Quantitative Spectroscopy and*
800 *Radiative Transfer*, 205, 51–58, <https://doi.org/10.1016/j.jqsrt.2017.09.032>, 2018.
- 801 Koshelev, M. A., Vilkov, I. N., Makarov, D. S., Tretyakov, M. Yu., Vispoel, B., Gamache, R. R., Cimini, D.,
802 Romano, F., and Rosenkranz, P. W.: Water vapor line profile at 183-GHz: Temperature dependence of broadening,
803 shifting, and speed-dependent shape parameters, *Journal of Quantitative Spectroscopy and Radiative Transfer*, 262,
804 107472, <https://doi.org/10.1016/j.jqsrt.2020.107472>, 2021.
- 805 Koshelev, M. A., Golubiatnikov, G. Yu., Vilkov, I. N., and Tretyakov, M. Yu.: Molecular oxygen fine structure
806 with sub-kHz accuracy, *Journal of Quantitative Spectroscopy and Radiative Transfer*, 278, 108001,
807 <https://doi.org/10.1016/j.jqsrt.2021.108001>, 2022.
- 808 Larosa, S., Cimini, D., Gallucci, D., Di Paola, F., Nilo, S. T., Ricciardelli, E., Ripepi, E., and Romano, F.: A Cloud
809 Detection Neural Network Approach for the Next Generation Microwave Sounder Aboard EPS MetOp-SG A1,
810 *Remote Sensing*, 15, 1798, <https://doi.org/10.3390/rs15071798>, 2023.
- 811 Liebe, H. J.: MPM—An atmospheric millimeter-wave propagation model, *Int J Infrared Milli Waves*, 10, 631–650,
812 <https://doi.org/10.1007/BF01009565>, 1989.
- 813 Liebe, H. J., Hufford, G. A., and Manabe, T.: A model for the complex permittivity of water at frequencies below
814 1 THz, *Int J Infrared Milli Waves*, 12, 659–675, <https://doi.org/10.1007/BF01008897>, 1991.
- 815 Liebe, H. J., Hufford, G. A., and Cotton, M.: Propagation modeling of moist air and suspended water/ice particles
816 at frequencies below 1000 GHz, In AGARD, 1993.
- 817 Liljegren, J. C., Boukabara, S.-A., Cady-Pereira, K., and Clough, S. A.: The effect of the half-width of the 22-GHz
818 water vapor line on retrievals of temperature and water vapor profiles with a 12-channel microwave radiometer,
819 *IEEE Transactions on Geoscience and Remote Sensing*, 43, 1102–1108,
820 <https://doi.org/10.1109/TGRS.2004.839593>, 2005.



- 821 Löhnert, U. and Maier, O.: Operational profiling of temperature using ground-based microwave radiometry at
822 Payerne: prospects and challenges, *Atmospheric Measurement Techniques*, 5, 1121–1134,
823 <https://doi.org/10.5194/amt-5-1121-2012>, 2012.
- 824 Makarov, D. S., Tretyakov, M. Yu., and Rosenkranz, P. W.: Revision of the 60-GHz atmospheric oxygen
825 absorption band models for practical use, *Journal of Quantitative Spectroscopy and Radiative Transfer*, 243,
826 106798, <https://doi.org/10.1016/j.jqsrt.2019.106798>, 2020.
- 827 Martinet, P., Cimini, D., De Angelis, F., Canut, G., Unger, V., Guillot, R., Tzanos, D., and Paci, A.: Combining
828 ground-based microwave radiometer and the AROME convective scale model through 1DVAR retrievals in
829 complex terrain: an Alpine valley case study, *Atmospheric Measurement Techniques*, 10, 3385–3402,
830 <https://doi.org/10.5194/amt-10-3385-2017>, 2017.
- 831 Martinet, P., Cimini, D., Burnet, F., Ménétrier, B., Michel, Y., and Unger, V.: Improvement of numerical weather
832 prediction model analysis during fog conditions through the assimilation of ground-based microwave radiometer
833 observations: a 1D-Var study, *Atmospheric Measurement Techniques*, 13, 6593–6611,
834 <https://doi.org/10.5194/amt-13-6593-2020>, 2020.
- 835 Marzano, F. S., Mugnai, A., Panegrossi, G., Pierdicca, N., Smith, E. A., and Turk, J.: Bayesian estimation of
836 precipitating cloud parameters from combined measurements of spaceborne microwave radiometer and radar, *IEEE
837 Transactions on Geoscience and Remote Sensing*, 37, 596–613, <https://doi.org/10.1109/36.739124>, 1999.
- 838 Matricardi, M.: The generation of RTTOV regression coefficients for IASI and AIRS using a new profile training
839 set and a new line-by-line database, *ECMWF Technical Memoranda*, 47, <https://doi.org/10.21957/59u3oc9es>,
840 2008.
- 841 Mech, M., Maahn, M., Kneifel, S., Ori, D., Orlandi, E., Kollias, P., Schemann, V., and Crewell, S.: PAMTRA 1.0:
842 the Passive and Active Microwave radiative TRAnsfer tool for simulating radiometer and radar measurements of
843 the cloudy atmosphere, *Geoscientific Model Development*, 13, 4229–4251, [https://doi.org/10.5194/gmd-13-4229-
844 2020](https://doi.org/10.5194/gmd-13-4229-2020), 2020.
- 845 Mlawer, E. J., Payne, V. H., Moncet, J.-L., Delamere, J. S., Alvarado, M. J., and Tobin, D. C.: Development and
846 recent evaluation of the MT_CKD model of continuum absorption, *Philosophical Transactions of the Royal Society
847 A: Mathematical, Physical and Engineering Sciences*, 370, 2520–2556, <https://doi.org/10.1098/rsta.2011.0295>,
848 2012.
- 849 Mollière, P., Wardenier, J. P., Boekel, R. van, Henning, T., Molaverdikhani, K., and Snellen, I. a. G.:
850 petitRADTRANS - A Python radiative transfer package for exoplanet characterization and retrieval, *A&A*, 627,
851 A67, <https://doi.org/10.1051/0004-6361/201935470>, 2019.
- 852 Moradi, I., Ferraro, R. R., Eriksson, P., and Weng, F.: Intercalibration and Validation of Observations From ATMS
853 and SAPHIR Microwave Sounders, *IEEE Transactions on Geoscience and Remote Sensing*, 53, 5915–5925,
854 <https://doi.org/10.1109/TGRS.2015.2427165>, 2015.



- 855 Payne, V. H., Delamere, J. S., Cady-Pereira, K. E., Gamache, R. R., Moncet, J.-L., Mlawer, E. J., and Clough, S.
856 A.: Air-Broadened Half-Widths of the 22- and 183-GHz Water-Vapor Lines, *IEEE Transactions on Geoscience*
857 *and Remote Sensing*, 46, 3601–3617, <https://doi.org/10.1109/TGRS.2008.2002435>, 2008.
- 858 Petty, G. W.: *A First Course in Atmospheric Radiation*, Sundog Pub., 2006.
- 859 Picard, G., Brucker, L., Fily, M., Gallée, H., and Krinner, G.: Modeling time series of microwave brightness
860 temperature in Antarctica, *Journal of Glaciology*, 55, 537–551, <https://doi.org/10.3189/002214309788816678>,
861 2009.
- 862 Picard, G., Sandells, M., and Löwe, H.: SMRT: an active–passive microwave radiative transfer model for snow
863 with multiple microstructure and scattering formulations (v1.0), *Geoscientific Model Development*, 11, 2763–
864 2788, <https://doi.org/10.5194/gmd-11-2763-2018>, 2018.
- 865 Rosenkranz, P.: *Absorption of Microwaves by Atmospheric Gases*, John Wiley and Sons, 1993.
- 866 Rosenkranz, P.: Line-by-line microwave radiative transfer (non-scattering), , <https://doi.org/10.21982/M81013>,
867 2017.
- 868 Rosenkranz, P. W.: Interference coefficients for overlapping oxygen lines in air, *Journal of Quantitative*
869 *Spectroscopy and Radiative Transfer*, 39, 287–297, [https://doi.org/10.1016/0022-4073\(88\)90004-0](https://doi.org/10.1016/0022-4073(88)90004-0), 1988.
- 870 Rosenkranz, P. W.: Water vapor microwave continuum absorption: A comparison of measurements and models,
871 *Radio Science*, 33, 919–928, <https://doi.org/10.1029/98RS01182>, 1998.
- 872 Rosenkranz, P. W.: Retrieval of temperature and moisture profiles from AMSU-A and AMSU-B measurements,
873 *IEEE Transactions on Geoscience and Remote Sensing*, 39, 2429–2435, <https://doi.org/10.1109/36.964979>, 2001.
- 874 Rosenkranz, P. W.: Comment on “Uncertainties in the temperature dependence of the line-coupling parameters of
875 the microwave oxygen band: impact study,” *IEEE Transactions on Geoscience and Remote Sensing*, 43, 2160–
876 2161, <https://doi.org/10.1109/TGRS.2005.853189>, 2005.
- 877 Rosenkranz, P. W.: A Model for the Complex Dielectric Constant of Supercooled Liquid Water at Microwave
878 Frequencies, *IEEE Transactions on Geoscience and Remote Sensing*, 53, 1387–1393,
879 <https://doi.org/10.1109/TGRS.2014.2339015>, 2015.
- 880 Rosenkranz, P. W., Cimini, D., Koshelev, M. A., and Tretyakov, M. Yu.: Covariances of Spectroscopic Parameter
881 Uncertainties in Microwave Forward Models and Consequences for Remote Sensing, in: 2018 IEEE 15th Specialist
882 Meeting on Microwave Radiometry and Remote Sensing of the Environment (MicroRad), 2018 IEEE 15th
883 Specialist Meeting on Microwave Radiometry and Remote Sensing of the Environment (MicroRad), 1–6,
884 <https://doi.org/10.1109/MICRORAD.2018.8430729>, 2018.



- 885 Rosenkranz, P. W. and Cimini, D.: Speed Dependence of 22- and 118-GHz Line Shapes for Tropospheric Remote
886 Sensing, *IEEE Transactions on Geoscience and Remote Sensing*, 57, 9702–9708,
887 <https://doi.org/10.1109/TGRS.2019.2928570>, 2019.
- 888 Rothman, L. S., Jacquemart, D., Barbe, A., Chris Benner, D., Birk, M., Brown, L. R., Carleer, M. R., Chackerian,
889 C., Chance, K., Coudert, L. H., Dana, V., Devi, V. M., Flaud, J.-M., Gamache, R. R., Goldman, A., Hartmann, J.-
890 M., Jucks, K. W., Maki, A. G., Mandin, J.-Y., Massie, S. T., Orphal, J., Perrin, A., Rinsland, C. P., Smith, M. A.
891 H., Tennyson, J., Tolchenov, R. N., Toth, R. A., Vander Auwera, J., Varanasi, P., and Wagner, G.: The HITRAN
892 2004 molecular spectroscopic database, *Journal of Quantitative Spectroscopy and Radiative Transfer*, 96, 139–204,
893 <https://doi.org/10.1016/j.jqsrt.2004.10.008>, 2005.
- 894 Rufenacht, R., Haeefe, A., Pospichal, B., Cimini, D., Bircher-Adrot, S., Turp, M., and Sugier, J.: EUMETNET
895 opens to microwave radiometers for operational thermodynamical profiling in Europe, *Bull. of Atmos. Sci.&*
896 *Technol.*, 2, 4, <https://doi.org/10.1007/s42865-021-00033-w>, 2021.
- 897 Sanò, P., Panegrossi, G., Casella, D., Di Paola, F., Milani, L., Mugnai, A., Petracca, M., and Dietrich, S.: The
898 Passive microwave Neural network Precipitation Retrieval (PNPR) algorithm for AMSU/MHS observations:
899 description and application to European case studies, *Atmospheric Measurement Techniques*, 8, 837–857,
900 <https://doi.org/10.5194/amt-8-837-2015>, 2015.
- 901 Saunders, R., Hocking, J., Turner, E., Rayer, P., Rundle, D., Brunel, P., Vidot, J., Roquet, P., Matricardi, M., Geer,
902 A., Bormann, N., and Lupu, C.: An update on the RTTOV fast radiative transfer model (currently at version 12),
903 *Geoscientific Model Development*, 11, 2717–2737, <https://doi.org/10.5194/gmd-11-2717-2018>, 2018.
- 904 Schreier, F., Gimeno García, S., Hedelt, P., Hess, M., Mendrok, J., Vasquez, M., and Xu, J.: GARLIC — A general
905 purpose atmospheric radiative transfer line-by-line infrared-microwave code: Implementation and evaluation,
906 *Journal of Quantitative Spectroscopy and Radiative Transfer*, 137, 29–50,
907 <https://doi.org/10.1016/j.jqsrt.2013.11.018>, 2014.
- 908 Schreier, F., Gimeno García, S., Hochstaffl, P., and Städt, S.: Py4CAts—PYthon for Computational ATmospheric
909 Spectroscopy, *Atmosphere*, 10, 262, <https://doi.org/10.3390/atmos10050262>, 2019.
- 910 Schroeder, J. A. and Westwater, E. R.: Users’ guide to WPL microwave radiative transfer software, 1991.
- 911 Shrestha, B., Brotzge, J. A., and Wang, J.: Evaluation of the New York State Mesonet Profiler Network data,
912 *Atmospheric Measurement Techniques*, 15, 6011–6033, <https://doi.org/10.5194/amt-15-6011-2022>, 2022.
- 913 Titos, G., Jefferson, A., Sheridan, P. J., Andrews, E., Lyamani, H., Alados-Arboledas, L., and Ogren, J. A.: Aerosol
914 light-scattering enhancement due to water uptake during the TCAP campaign, *Atmospheric Chemistry and Physics*,
915 14, 7031–7043, <https://doi.org/10.5194/acp-14-7031-2014>, 2014.



- 916 Tretyakov, M. Y., Parshin, V. V., Koshelev, M. A., Shanin, V. N., Myasnikova, S. E., and Krupnov, A. F.: Studies
917 of 183GHz water line: broadening and shifting by air, N₂ and O₂ and integral intensity measurements, *Journal of*
918 *Molecular Spectroscopy*, 218, 239–245, [https://doi.org/10.1016/S0022-2852\(02\)00084-X](https://doi.org/10.1016/S0022-2852(02)00084-X), 2003.
- 919 Tretyakov, M. Yu.: Spectroscopy underlying microwave remote sensing of atmospheric water vapor, *Journal of*
920 *Molecular Spectroscopy*, 328, 7–26, <https://doi.org/10.1016/j.jms.2016.06.006>, 2016.
- 921 Tretyakov, M. Yu., Koshelev, M. A., Dorovskikh, V. V., Makarov, D. S., and Rosenkranz, P. W.: 60-GHz oxygen
922 band: precise broadening and central frequencies of fine-structure lines, absolute absorption profile at atmospheric
923 pressure, and revision of mixing coefficients, *Journal of Molecular Spectroscopy*, 231, 1–14,
924 <https://doi.org/10.1016/j.jms.2004.11.011>, 2005.
- 925 Tripoli, G. J., Medaglia, C. M., Dietrich, S., Mugnai, A., Panegrossi, G., Pinori, S., and Smith, E. A.: The 9–10
926 November 2001 Algerian Flood: A Numerical Study, *Bulletin of the American Meteorological Society*, 86, 1229–
927 1235, 2005.
- 928 Tritsis, A., Yorke, H., and Tassis, K.: Python Radiative Transfer Emission code (pyrate): non-local thermodynamic
929 equilibrium spectral lines simulations, *Monthly Notices of the Royal Astronomical Society*, 478, 2056–2064,
930 <https://doi.org/10.1093/mnras/sty1152>, 2018.
- 931 Turner, D. D. and Löhnert, U.: Ground-based temperature and humidity profiling: combining active and passive
932 remote sensors, *Atmospheric Measurement Techniques*, 14, 3033–3048, [https://doi.org/10.5194/amt-14-3033-](https://doi.org/10.5194/amt-14-3033-2021)
933 2021, 2021.
- 934 Turner, D. D., Cadeddu, M. P., Löhnert, U., Crewell, S., and Vogelmann, A. M.: Modifications to the Water Vapor
935 Continuum in the Microwave Suggested by Ground-Based 150-GHz Observations, *IEEE Transactions on*
936 *Geoscience and Remote Sensing*, 47, 3326–3337, <https://doi.org/10.1109/TGRS.2009.2022262>, 2009.
- 937 Turner, E., Rayer, P., and Saunders, R.: AMSUTRAN: A microwave transmittance code for satellite remote
938 sensing, *Journal of Quantitative Spectroscopy and Radiative Transfer*, 227, 117–129,
939 <https://doi.org/10.1016/j.jqsrt.2019.02.013>, 2019.
- 940 Vermote, E. F., Tanre, D., Deuze, J. L., Herman, M., and Morcette, J.-J.: Second Simulation of the Satellite Signal
941 in the Solar Spectrum, 6S: an overview, *IEEE Transactions on Geoscience and Remote Sensing*, 35, 675–686,
942 <https://doi.org/10.1109/36.581987>, 1997.
- 943 Wang, D., Prigent, C., Kilic, L., Fox, S., Harlow, C., Jimenez, C., Aires, F., Grassotti, C., and Karbou, F.: Surface
944 Emissivity at Microwaves to Millimeter Waves over Polar Regions: Parameterization and Evaluation with Aircraft
945 Experiments, *Journal of Atmospheric and Oceanic Technology*, 34, 1039–1059, [https://doi.org/10.1175/JTECH-](https://doi.org/10.1175/JTECH-D-16-0188.1)
946 D-16-0188.1, 2017.



- 947 Wei, S.-W., Lu, C.-H. (Sarah), Johnson, B. T., Dang, C., Stegmann, P., Grogan, D., Ge, G., and Hu, M.: The
948 Influence of Aerosols on Satellite Infrared Radiance Simulations and Jacobians: Numerical Experiments of CRTM
949 and GSI, Remote Sensing, 14, 683, <https://doi.org/10.3390/rs14030683>, 2022.
- 950 Wilson, R. T.: Py6S: A Python interface to the 6S radiative transfer model, Computers & Geosciences, 51, 166–
951 171, <https://doi.org/10.1016/j.cageo.2012.08.002>, 2013.